Czech Technical University in Prague
Faculty of Nuclear Sciences and Physical Engineering
Department of Physics

Study of jet substructure in Au+Au collisions with the STAR experiment

RESEARCH PROJECT

Author: Bc. Monika Robotková
Supervisor: RNDr. Jana Bielčíková, Ph.D.
Year: 2020

České vysoké učení technické v Praze
Fakulta jaderná a fyzikálně inženýrská
Katedra fyziky

Studium substruktury jetů v Au+Au srážkách v experimentu STAR

VÝZKUMNÝ ÚKOL

Vypracovala:	Bc. Monika Robotková
Vedoucí práce:	RNDr. Jana Bielčíková, Ph.D.
Rok:	2020

ČESKÉ VYSOKÉ UČENÍ TECHNICKÉ V PRAZE
FAKULTA JADERNÁ A FYZIKÁLNĚ INŽENÝRSKÁ
PRAHA 1 - STARÉ MĚSTO, BŘEHOVÁ 7 - PSČ 115 19

Katedra: fyziky **Akademický rok:** 2019/2020

VÝZKUMNÝ ÚKOL

Student: **Bc. Monika Robotková**

Studijní program: **Aplikace přírodních věd**

Obor: **Experimentální jaderná a částicová fyzika**

Vedoucí úkolu: **RNDr. Jana Bielčíková, Ph.D.**

Název úkolu (česky/anglicky):

Studium substruktury jetů v Au+Au srážkách v experimentu STAR

Study of jet substructure in Au+Au collisions with the STAR experiment

Pokyny pro vypracování:

1. Přehled aktuálních výsledků měření vlastností jetů v jádro-jaderných srážkách na urychlovačích RHIC a LHC.
2. Popis experimentu STAR na urychlovači RHIC a jeho detektorů.
3. Rekonstrukce jetů a aplikace techniky "soft-drop" pro deklasterizaci jetů na data z Au+Au srážek při energii 200 GeV na nukleon-nukleonový pár.
4. Studium pozorovatelných z_g a R_g popisujících substrukturu jetu v závislosti na příčné hybnosti jetu, rozlišovacím parametru a centralitě Au+Au srážky.

Výzkumný úkol bude vypracován v anglickém jazyce.
Součástí zadání výzkumného úkolu je jeho uložení na webové stránky katedry fyziky.

Literatura:

1. K. Yagi, et al: Quark-gluon plasma, Cambridge University Press, 2005
2. M. Cacciari, G. P. Salam and G. Soyez: FastJet User Manual, Eur. Phys. J C72 (2012) 1896
3. A. J. Larkoski, S. Marzani, G. Soyez and J. Thaler: Soft Drop, JHEP 05 (2014) 146
4. ALICE Collaboration: Exploration of jet substructure using iterative declustering in pp and Pb-Pb collisionsat LHC energies, arXiv 1905.02512

Datum zadání: 25.10.2019 ....

Datum odevzdání: 26.06.2020 ***vedoucí katedry***

Prohlášení

Prohlašuji, že jsem svůj výzkumný úkol vypracovala samostatně a použila jsem pouze podklady (literaturu, projekty, SW atd.) uvedené v přiloženém seznamu.

Nemám závažný důvod proti použití školního díla ve smyslu § 60 Zákona č. 121/2000 Sb., o právu autorském, o právech souvisejících s právem autorským a o změně některých zákonů (autorský zákon).

V Praze dne ....

Bc. Monika Robotková

Acknowledgement

I would like to thank RNDr. Jana Bielčíková, Ph.D. for guiding this thesis, professional advice, language correction and, above all, for her patience. I would also like to thank my colleagues for their valuable advice and help with analysis.

Bc. Monika Robotková

Název práce:
Studium substruktury jetů v Au+Au srážkách v experimentu STAR

Autor: Bc. Monika Robotková

Studijní program: Aplikace přírodních věd
Obor: Experimentální jaderná a částicová fyzika
Druh práce: Výzkumný úkol

Vedoucí práce: RNDr. Jana Bielčíková, Ph.D.
Ústav jaderné fyziky AV ČR, v.v.i.

Abstrakt: Kvark-gluonové plazma vzniká ve srážkách těžkých iontů při vysokých energiích. Jednou z možností, jak tuto horkou hustou hmotu zkoumat, je prostřednictvím jetů. Tato práce se zaměřuje především na substrukturu jetů, konkrétně na pozorovatelné z_g (angl. *Shared Momentum Fraction*) a R_g (angl. *Groomed Jet Radius*). Jsou zde také představeny různé metody odečtu pozadí, které jsou využity během analýzy. Analýza představená v této práci proběhla na datech ze srážek Au+Au naměřených experimentem STAR v roce 2014 při těžišťové energii na nukleonový pár $\sqrt{s_{NN}} = 200$ GeV.
Klíčová slova: kvark-gluonové plazma, jet, jetová substruktura, STAR experiment, odečet pozadí

Title:
Study of jet substructure in Au+Au collisions with the STAR experiment

Author: Bc. Monika Robotková

Abstract: Quark-gluon plasma is formed in heavy ion collisions at high energies. One way to study this hot, dense matter is through jets. This work focuses mainly on the substructure of jets, specifically on the observables Shared Momentum Fraction z_g and Groomed Jet Radius R_g. Background subtraction methods used in this analysis are also introduced. The analysis presented in this thesis was applied on data collected in Au+Au collisions at the center of mass energy per nucleon pair $\sqrt{s_{NN}} = 200$ GeV measured by the STAR experiment in 2014.
Key words: quark-gluon plasma, jet, jet substructure, STAR experiment, background subtraction

Contents

List of Figures

Introduction

Quark-gluon plasma (QGP) is a hot dense matter that occurred in space shortly after the Big Bang and can now be formed by ultra-relativistic collisions of heavy ions. QGP is investigated on particle accelerators such as the Relativistic Heavy Ion Collider (RHIC) in Brookhaven National Laboratory (BNL) and Large Hadron Collider (LHC) in CERN. One of the possible probes used to study QGP are jets that originate from hard partonic collisions in the early stage of collisions.

Jets are collimated sprays of hadrons, which we describe using algorithms. As jets pass through the medium, they may be modified. This modification is called jet quenching. Thanks to these modifications, we can study the nuclear medium more closely. We can look at jets in several ways, for example in terms of their inclusive properties or study their substructure, which is the topic of this thesis.

The first chapter describes the basic principles of heavy ion collisions and also some quantities that characterize these collisions. Furthermore, the quark-gluon plasma is presented, the possibilities of its formation and its evolution in time and space are described.

The second chapter presents RHIC, located at Brookhaven National Laboratory, where heavy ion collisions are performed. The major part of this chapter is then devoted to the STAR experiment located at RHIC and its subdetectors which were used to perform analysis in this thesis.

In the third chapter, the reader gets acquainted with jets as well as with the algorithms used to reconstruct them. This is followed by the fourth chapter, which deals with the substructure of jets and techniques that can be used in the study of substructure. In particular, in the fourth chapter are discussed the observables shared momentum fraction z_g and groomed jet radius R_g, which are the main subject of research in this thesis.

The fifth chapter presents the principles of background subtraction methods that are used in the analysis. Namely, they are Area-Based Subtraction, Constituent Background Subtraction and SoftKiller.

Chapter 6 contains a description of the practical part of this work, which includes the analysis of data measured from Au+Au collisions at energy $\sqrt{s_{NN}} = 200$ GeV per nucleon pair. The principles of event analysis, jet reconstruction and subsequent application of methods for background subtraction are described here. The results of the current analysis are also presented.

The research thesis ends with a summary and outlook for the future in the field of jet analysis and the study of their substructure.

Chapter 1

Quark-Gluon Plasma

1.1 Heavy Ion Collision

By heavy ions are meant nuclei in heavy elements, especially metals. These collisions are usually performed on particle accelerators. The largest particle accelerators available to collide heavy ions and are currently under operation include the Relativistic Heavy Ion Collider (RHIC), where Au+Au collisions are mainly performed, and the Large Hadron Collider (LHC) at CERN, where Pb+Pb collisions take place.

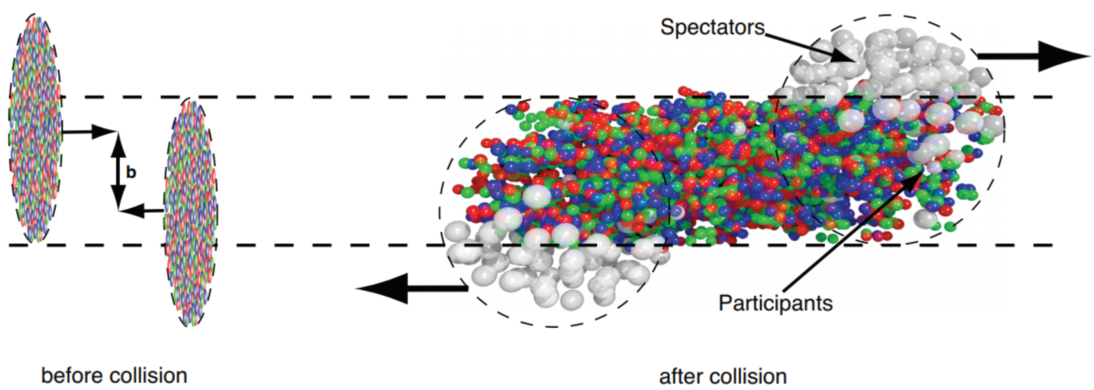

Figure 1.1: Two heavy nuclei with impact parameter b before and after collision [1].

1.1.1 Centrality

At high energies, relativistic phenomena occur in colliding nuclei, such as length contraction, which causes the nuclei to change shape into thin disks, as depicted in Fig. 1.1. For nuclei that look like this, it makes sense to introduce a quantity called centrality, which describes how much the nuclei overlap in a collision. Given that nuclei have disk shapes, it is clear that not all nucleons have to be directly involved in the collision. Based on this, we can divide nucleons into so-called **participants**,

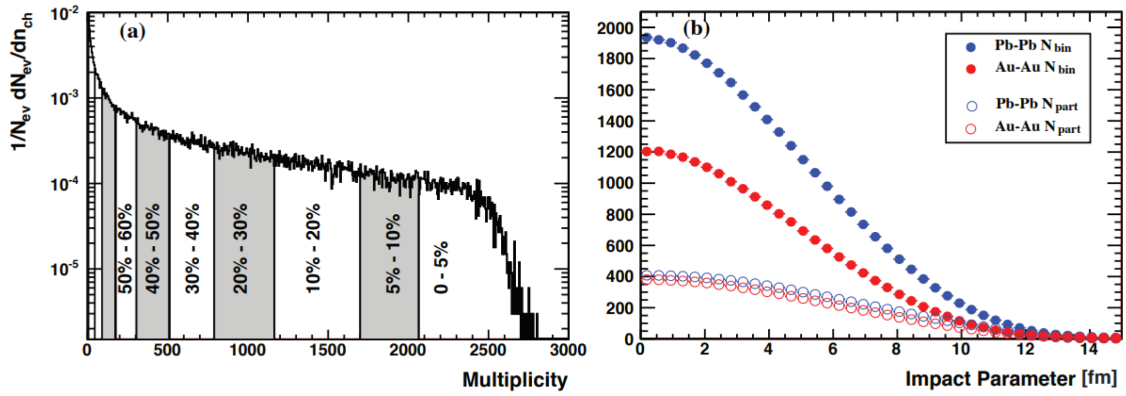

Figure 1.2: a) Charged particle distribution in Pb+Pb collision at $\sqrt{s_{NN}} = 2.76$ TeV measured by the ALICE experiment together with centrality classification. b) Number of participants and binary collisions depending on the impact parameter b in Au+Au ($\sqrt{s_{NN}} = 0.2$ TeV) and Pb+Pb ($\sqrt{s_{NN}} = 2.76$ TeV) collisions calculated in the Glauber model [1].

who participate in the collision, and **spectators**, who do not. The quantity that is used to express the overlapping region of the colliding nuclei is called centrality and is defined as

$$c_b \equiv \frac{1}{\sigma_{inel}} \int_0^b P_{inel}(b') 2\pi b' db', \tag{1.1}$$

where σ_{inel} is the inelastic cross section, b is the impact parameter which indicates the distance between the centers of the colliding nuclei and P_{inel} is the probability that an inelastic collision occurs at the impact parameter b.

Nuclear collisions can then be classified into three groups based on the size of the impact parameter. The first group consists of central collisions, for which $b \approx 0$. The second group is called peripheral collisions and $0 < b < 2R$ applies to them, where R is the radius of the nucleus. The last group is called ultra-peripheral collisions and the impact parameter in this case satisfies $b > 2R$.

Experimentally, the centrality of the collision is determined, for example, from the measured multiplicity of particles produced, which is a function of the parameter b. The results of measurements from Pb+Pb collisions and the distribution of centralities are shown in Fig. 1.1. In the graph on the left we see that the intervals of centralities are determined by what percentage of the total multiplicity they cover.

1.1.2 Glauber model

The impact parameter b is one of the geometric observables used to describe the relativistic collisions of heavy ions. These variables also include, for example, the number of participants in the collision N_{part} and the number of binary, nucleon-nucleon, collisions N_{coll}. Unfortunately, none of these observables can be measured directly and the Glauber model [2] is used to determine them.

We should however keep in mind, that it is only a model and several approximations are used. One of them is the assumption that the energy of nucleons is high, thanks to which the nucleons move along straight trajectories. Another assumption is that the nucleons move independently in the nucleus and the force acting between the nucleons is small relative to the size of the nucleus.

When these assumptions are met, the observable N_{part} is defined as

$$N_{part}(b) = \int d^2 s T_A(s)(1 - e^{-\sigma_{NN}^{inel} T_B(s)}) + \int d^2 s T_B(s-b)(1 - e^{-\sigma_{NN}^{inel} T_A(s)}), \quad (1.2)$$

where T_A is function of the nucleus thickness defined as $T_A(s) = \int dz \rho_A(z,s)$, where z axis in the direction of the beam, b is impact parameter, s is the distance drawn in Fig. 1.3, ρ_A is the nucleon density usually determined by Wood-Saxon distribution and σ_{NN}^{inel} is an inelastic cross section. Because the motion of nucleons is independent of the nucleus and secondary particle production is not considered in the model, the cross section is the same as in a vacuum.

Next, the observable N_{coll} is defined in the Galuber model as follows:

$$N_{coll}(b) = \int d^2 s T_B(s-b) \sigma_{NN}^{inel} T_A(s). \quad (1.3)$$

The dependence of N_{part} and N_{coll} on the impact parameter b is shown in Fig. 1.1 on the right. The graph shows the Glauber model calculations for Pb+Pb collisions at $\sqrt{s_{NN}} = 2.76$ TeV and Au+Au collisions at $\sqrt{s_{NN}} = 0.2$ TeV.

1.2 Quark-Gluon Plasma formation

One of the reasons why heavy ion collisions are being investigated is the possibility of forming a nuclear matter called Quark-Gluon Plasma (QGP). The formation of QGP is conditioned by extremely high temperature and/or density. It is assumed that QGP was formed for a very short time immediately after the Big Bang. At present, QGP could be present in the center of compact stars or could be created in laboratory in aforementioned heavy ion collisions.

Under normal conditions, quarks are bound together by a strong interaction mediated by gluons. The strong interaction is described by a theory called quantum chromodynamics (QCD).

QCD provides us with two important insights. The first of these is the weakening of the interaction between quarks and gluons with increasing energy, when the so-called asymptotic freedom occurs. In this state, free quarks and gluons can form

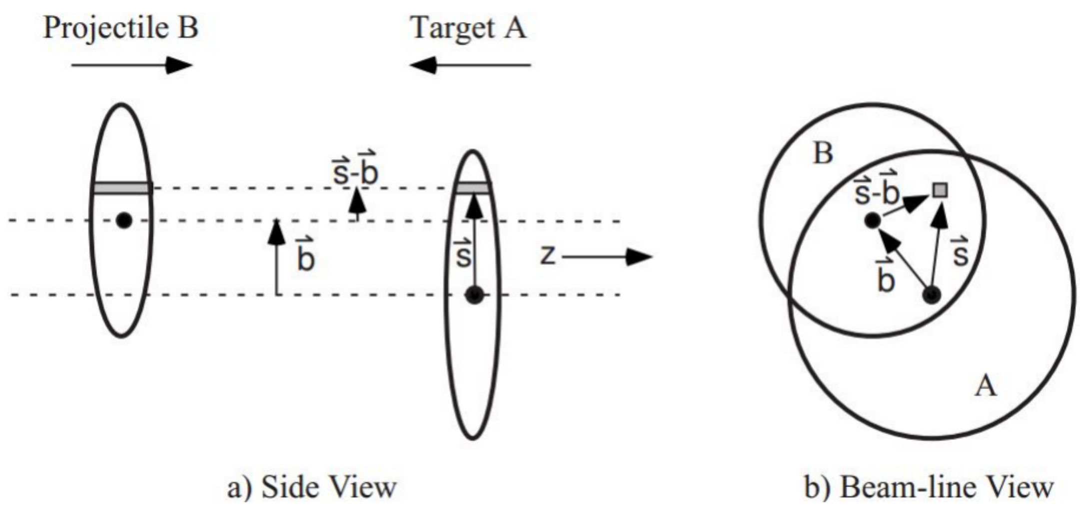

Figure 1.3: Collision geometry scheme in the Glauber model. a) side view, b) beam-line view [2].

QGP. On the contrary, at low energies, the interaction between quarks and gluons is strong and the so-called color confinement [3].

Fig. 1.4 shows the QGP phase diagram. It displays the dependence of temperature T on the baryochemical potential μ_B, which indicates the balance between matter and antimatter. For $\mu_B = 0$, the transition temperature between QGP and hadron gas is approximately equal to $T_c \simeq 170$ MeV. At low baryon density, the transition is not accompanied by discontinuities of thermodynamic quantities. From a certain critical point, the first order phase transition takes place.

1.3 Space-time evolution of heavy ion collision

This section describes in more detail the space-time evolution of heavy ion collisions in which QGP is formed. This evolution is illustrated in Fig. 1.5. The development of the collision is then divided into three main phases.

Pre-equilibrium stage and thermalization

In the first phase of the collision at the time $\tau < \tau_0$ the so-called fireball arises, which is a non-equilibrium state producing high entropy. So far, two models of entropy production and subsequent thermalization have been published. The first of these is an incoherent model, according to which parton collisions produce minijets that interact with each other to produce parton media. The second, coherent model, proposes the formation of colored strings and ropes, which then decay into real partons and thermalize.

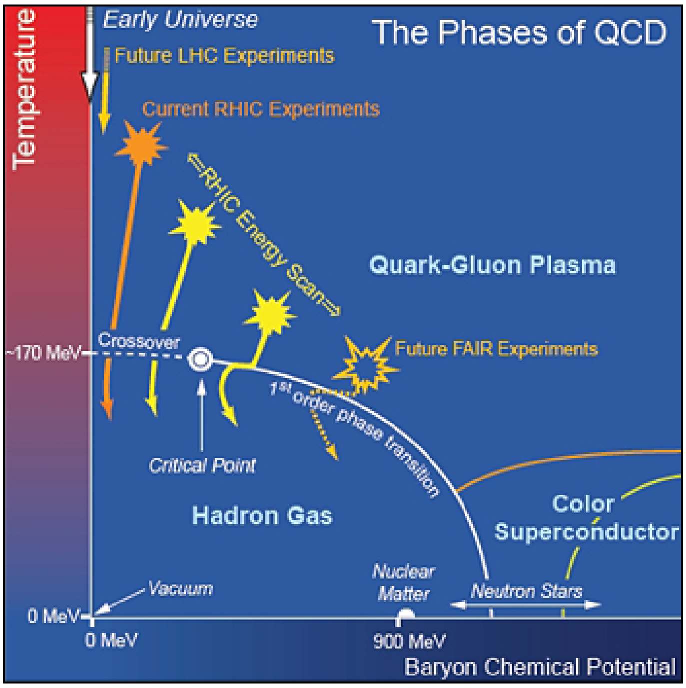

Figure 1.4: Phase diagram of strongly interacting nuclear matter [4].

Hydrodynamical evolution

At time $\tau_0 < \tau < \tau_f$, a thermalized quark-gluon plasma is formed, which expands very rapidly and also cools. When it reaches the critical temperature T_c, a phase transition to hadron gas takes place.

Freeze-out and post-equilibrium

In the last phase at the time $\tau = \tau_f$ the so-called freeze-out will take place. We divide this phase into chemical and kinetic freeze-out. The chemical freeze-out takes place earlier and during it the number of particles stabilizes, thus ceasing inelastic scattering. During kinetic freeze-out, elastic scattering no longer takes place. At the same time, the momentum of the hadrons stabilizes at a given value. These hadrons then travel to the detector.

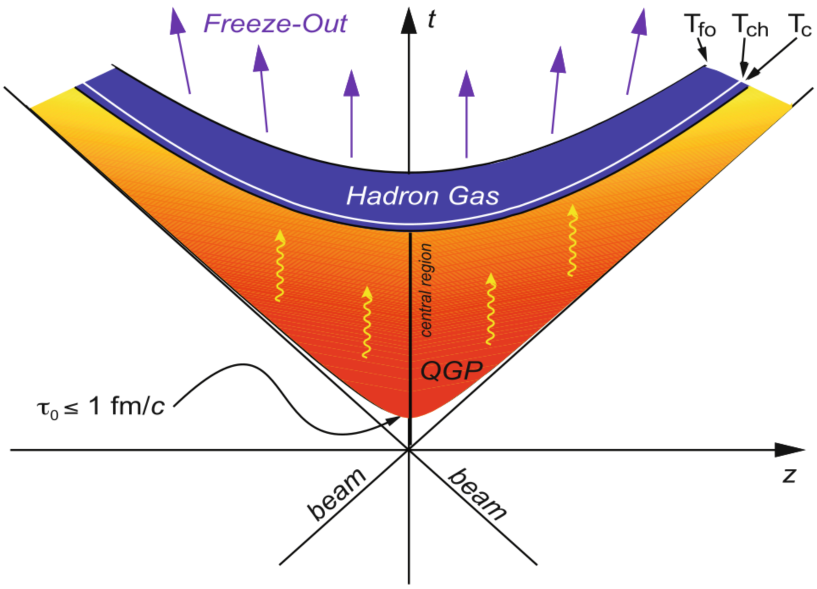

Figure 1.5: A space-time evolution of the heavy ion collision [5].

Chapter 2

RHIC and STAR

BNL (*Brookhaven National Laboratory*) is located on Long Island, New York. The laboratory was formally established in 1947 to support research in atomic energy. Currently, research at BNL focuses not only on physics, but also chemistry, biology and other disciplines. Many important discoveries have been made here, such as the observation of a quark-gluon plasma, the CP violation, and the discovery of several subatomic particles. So far, researchers working at BNL have been awarded 7 Nobel Prizes.

2.1 RHIC

RHIC (**R**elativistic **H**eavy **I**on **C**ollider) is a 3834 m long circular accelerator located at BNL. The accelerator has been operating since 2000 and has 4 main experiments on it: BRAHMS, PHENIX, PHOBOS and STAR.

Currently, only the STAR experiment is running, all others have already shut down. In 2022, a new sPHENIX experiment should be launched to replace the PHENIX experiment. The aim of this experiment will be to obtain a refinement of the results from the STAR and PHENIX experiments. [6].

Before heavy ions enter RHIC, they must be pre-accelerated by the BNL accelerator complex. Ions start they journey in the Electron Beam Ion Source (EBIS) where are highly charged ion beams accelerated by two Tandem van de Graaff accelerators. Ion beams are then carried to the Booster synchrotron. This circular accelerator provides ions with energy 95 MeV per nucleon. The next part of the complex into which the ions enter is called Alternating Gradient Synchrotron (AGS). Here, the ions are accelerated until they reach an energy of 8.86 GeV per nucleon. Finally, the ions go to the RHIC accelerator at 99.7% of the speed of light.

RHIC can also accelerate and collid protons. The principle of acceleration is very similar to that of ions, differing only at the beginning of the process, when EBIS is replaced by the Linear Proton Accelerator (LINAC). The protons from LINAC then enter the BOOSTER and subsequent acceleration process is the same as for the ions.

RHIC acceleration complex is shown in Fig.2.1.

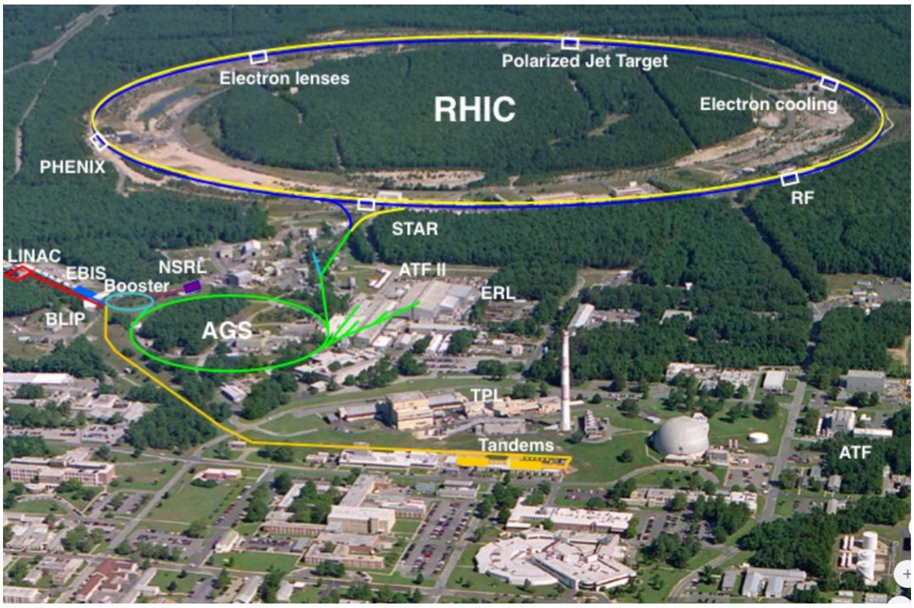

Figure 2.1: RHIC acceleration complex [7].

2.2 STAR

The STAR (**S**olenoidal **T**racker **A**t **R**HIC) is currently the only working experiment at RHIC accelerator. The main goal of the experiment is to study QGP and also to study the proton spin. Almost 700 employees from 67 different institutions from 14 countries are collaborating on the experiment [8].

The whole detector consists of several small subdetectors, each with its own specific function. From the data measured using these subdetectors, it is then possible to compose the complex image of the collision. The STAR detector with marked subdetectors is shown in Fig. 2.2. In the rest of this section, the individual subdetectors are described in more detail.

- **TPC** (*Time Projection Chamber*): forms the main part on the STAR experiment. It is a 4.2 m long cylinder with a diameter of 4 m. Thanks to this shape and size, it is able to cover the full azimuthal angle and pseudorapidity $|\eta| \leq 1$. The chamber is divided into two parts by a carbon membrane, which ensures a constant electric field in the chamber. As the charged particle passes through the chamber, the gas which fills the chamber is ionized. The generated electrons then drift to the ends of the chamber, where their signal is read by a set of MWPCs (Multi-Wire Proportional Chambers). This detector is designed to map particle tracks, measure their momenta and due to ionization energy loss it is possible to identify particles. A schematic drawing of the TPC is shown in Fig. 2.3.

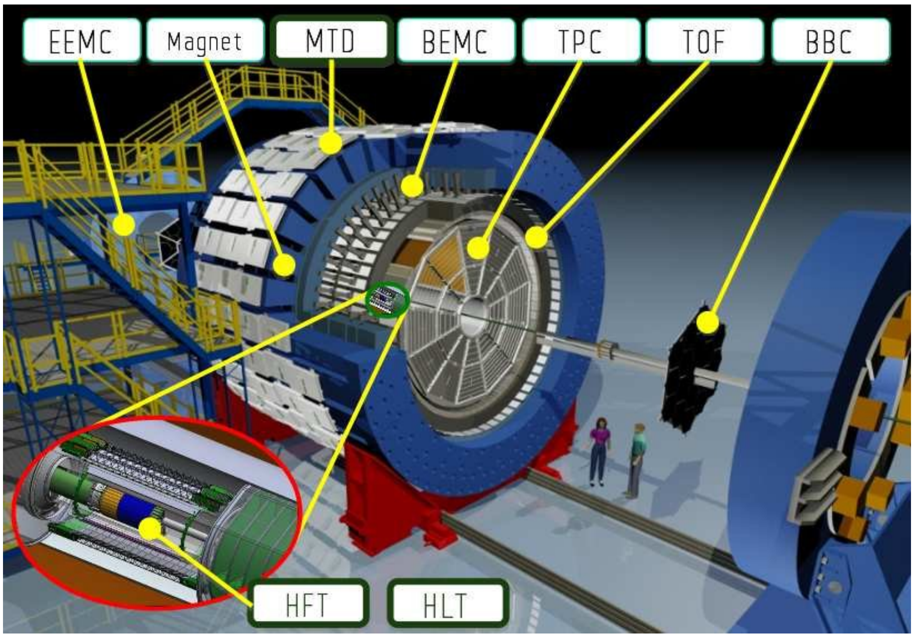

Figure 2.2: The STAR experiment with its subdetectors [9].

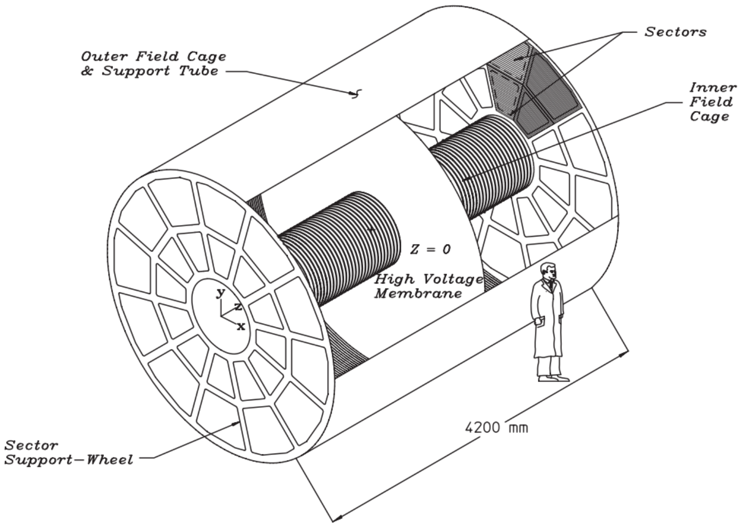

Figure 2.3: A schematic view of the Time Projection Chamber of the STAR experiment [10].

In 2019, the inner part of the TPC was upgraded with the so-called **iTPC** (inner Time Projection Chamber), thanks to which the TPC has now extended pseudorapidity coverage $|\eta| \leq 1.5$.

- **TOF** (*Time of Flight*): This detector is located around the TPC, so it again covers the full azimuthal angle and pseudorapidity $|\eta| < 1$. As the name suggests, the TOF is designed to measure the flight time of particles. From the measured data, it is then possible to identify particles based on their different velocities. In 2019, an **eTOF** (endcap Time of Flight) was added, which should serve to extend particle identification capabilities [11].

- **BEMC** (*Barrel Electromagnetic Calorimeter*): Another detector in the series is the BEMC. It is located above the TOF and is used to measure the deposited energy of neutral particles. The detector consists of 4800 towers, which consist of scintillation plates and lead plates. This detector again covers the full azimuthal angle and pseudorapidity $|\eta| < 1$. Together with the TOF detector, this detector serves as a trigger for high-energy events [12]. The schema of this detector is in Fig. 2.4.

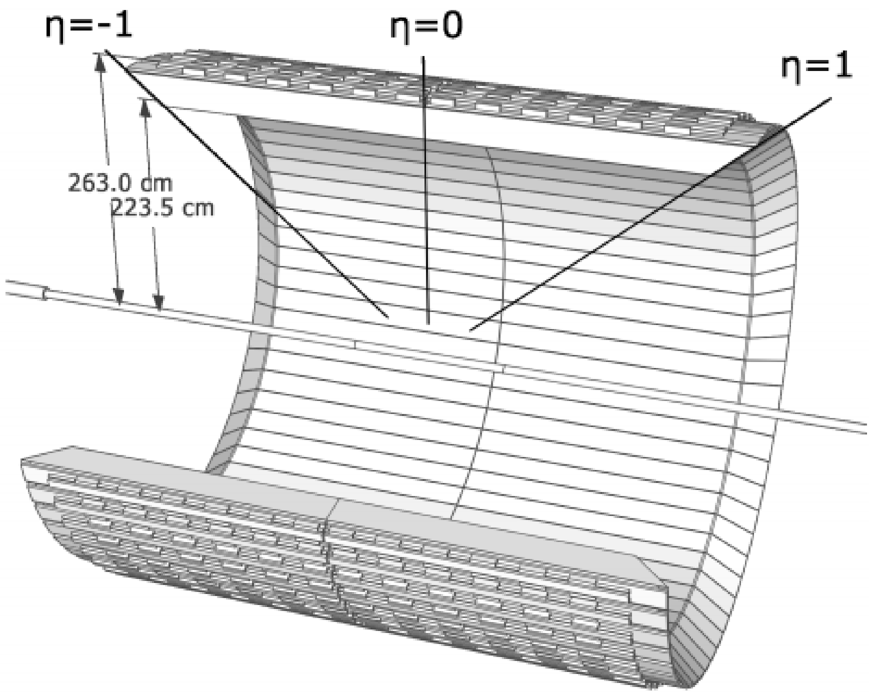

Figure 2.4: Drawing of BEMC detector [13].

- **EEMC** (*Endcap Electromagnetic Calorimeter*): The EEMC complements the BEMC detector and is located on the west side of the STAR experiment. EEMC covers the full azimuthal angle and pseudorapidity $1 < \eta \leq 2$ [14].

- **BBC** (*Beam-Beam Counter*): The main purpose of this detector is diagnostics for polarized proton beams. The detector is divided into two parts, which are 3.75 m away from the center of the STAR detector and are located at its opposite ends. [15].

- **VPD** (*Vertex Position Detector*): This detector is used to determine the location of the collision. It consists of two separate detectors, located on the west and east side of the STAR experiment 5.7 m from its center. It covers pseudorapidity $4.24 \leq \eta \leq 5.1$ [16].

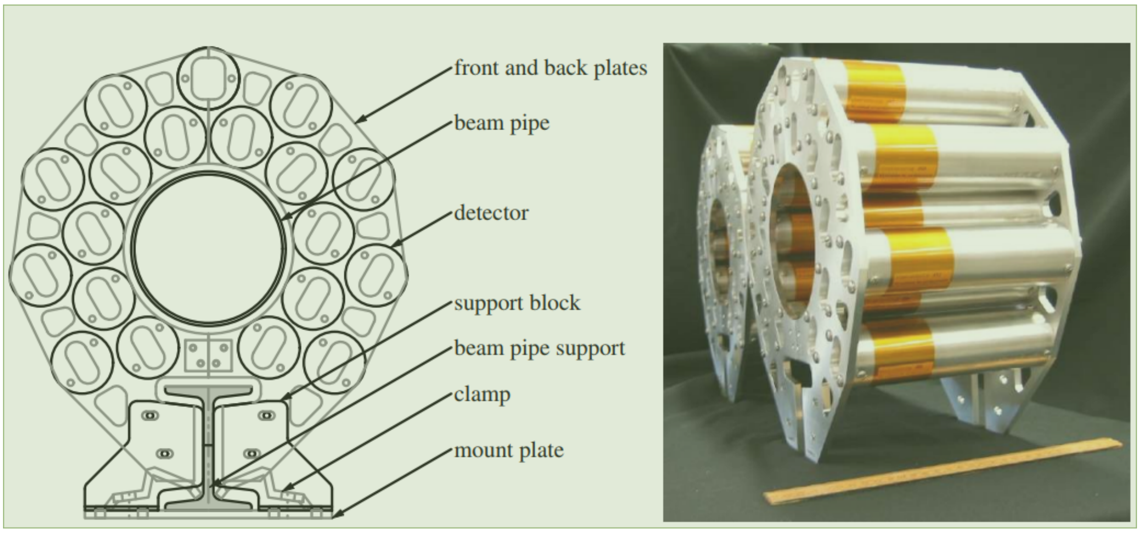

Figure 2.5: VPD detector [16].

- **ZDC** (*Zero Degree Calorimeters*): ZDC is important for the detection of neutrons flying out of a collision at a very small angle. It is also used to measure their total energy. This measurement is important mainly for the subsequent calculation of multiplicity. Like the VPD, this detector is divided into two parts, which are located at opposite ends of the STAR experiment 18 m from its center [17].

- **HFT** (*Heavy Flavor Tracker*): This detector was part of the STAR experiment only in the years 2014-2016. It was located closest to the beam and was used to reconstruct hadrons composed of heavy quarks. It consisted of four layers of silicon detectors and divided into the following three parts [18]:

  - SSD - a cylindrical strip detector located 23 cm from the beam axis,
  - IST - the middle part located 14 cm from the beam axis,
  - PXL - two layers of pixel detectors located at distances of 8 cm and 2.5 cm from the beam axis.

The detector is shown in Fig. 2.6.

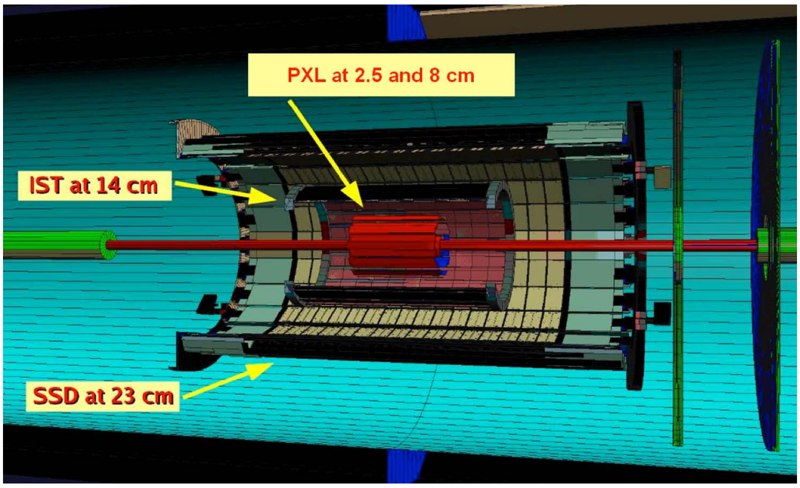

Figure 2.6: The HFT detector of the STAR experiment [19].

Chapter 3

Jets

A jet is a collimated spray of hadrons created by the fragmentation of high-energy partons. Immediately after the collision, the partons move for a short time as free particles, which produce bremsstrahlung when scattered. This radiation is in the form of gluons and quark-antiquark pairs. Then the color confinement occurs and collimated groups of hadrons are formed, which move in the direction of the original partons. Since the properties of jets reflect the properties of the original partons, we can obtain information about them, such as spin, flavor or color charge [20, 21].

Jets can be a good probe for quark-gluon plasma research, as the shape of the jet and its internal structure can be affected by the medium during heavy ion collisions. This phenomenon is called jet quenching.

3.1 Algorithms for jet reconstruction

Before the analysis itself, it is first necessary to reconstruct the jet from the output data from the detectors. Jet algorithms are used for this reconstruction. These algorithms can be generally divided into two main groups - conical and sequential clustering. All algorithms have their advantages and disadvantages, but in general they should meet the following conditions:

1. **Infrared and collinear safety**: the reconstructed jet should not change when the soft parton is radiated by the original parton or when the original parton is divided into two collinear partons.

2. **Applicability at all levels of analysis**: the algorithm should produce the same results when applied to theoretical calculations at the parton level, during simulations at the hadron level and when applied to the measured data from the detector.

3. **Detector independence**: the results of the algorithm used should not depend too much on the properties of the detector we use to collect data.

4. **High efficiency and short calculation time**: ideally, all jets should be reconstructed and the reconstruction time should be as short as possible.

5. **Easy to use**: the algorithm should be as easy to apply as possible for the user.

3.1.1 Sequential clustering algorithms

Since in the following analysis only sequential clustering algorithms are used for jet reconstruction, below we will describe the most common ones. All these algorithms are based on the principle of selecting one initial particle, to which others are then added until the final jet is formed. These algorithms include k_t, anti-k_t and C/A, which are described in more detail below. All of these algorithms are part of the FastJet [22] software package used to analyze jets.

k_t algorithm

The reconstruction process using the k_t algorithm consists of the following steps:

1. For each pair of particles i, j, the distance d_{ij} is calculated as

$$d_{ij} = \frac{\min(p_{Ti}^2, p_{Tj}^2)\Delta R_{ij}^2}{R}, \tag{3.1}$$

   where $\Delta R_{ij}^2 = (y_i - y_j)^2 + (\varphi_i - \varphi_j)^2$, p_{Ti} is transverse momentum, y_i rapidity, φ_i azimuthal angle of the particle i and R is resolution parameter. For each parton i the distance from the beam is further determined as $d_{iB} = p_{Ti}^2$.

2. We are looking for a minimum value among all d_{ij} and d_{iB}. If the minimum corresponds to d_{ij}, particles i and j are connected into one "protojet" by summing their four-momenta. If the minimum corresponds to d_{iB}, "protojet" i is considered as the final jet and removed from the current set of particles.

3. The whole procedure is repeated until no particles remain.

This algorithm first clusters soft particles, so it is most commonly used to determine the background energy density of the collision [22, 23].

Anti-k_t algorithm

The clustering procedure using the anti-k_t algorithm is essentially the same as for the k_t algorithm, the only difference being the definition of the distances d_{ij} and d_{iB}, which in the case of this algorithm are defined as follows:

$$d_{ij} = \frac{\min(1/p_{Ti}^2, 1/p_{Tj}^2)\Delta R_{ij}^2}{R}, \tag{3.2}$$

$$d_{iB} = 1/p_{Ti}^2. \tag{3.3}$$

This algorithm is most suitable for jet reconstruction. On the contrary, its use is not suitable if we want to study the substructure of the jet [22, 23].

Cambridge/Aachen (C/A) algorithm

For the C/A algorithm, the procedure is the same as in the previous two cases, but the distances are defined as $d_{ij} = \Delta R_{ij}^2/R^2$ and $d_{iB} = 1$.

Since in the case of this algorithm the transverse momentum of particles does not appear in the definition of distance, but only the spatial coordinates, this algorithm is the most suitable for declusterization. Therefore, it is often used in the study of jet substructure, which is the main subject of this research thesis [23].

In Fig. 3.1 we can see a graphical representation of the three described algorithms when applied to the same data using $R = 1$. At the top left we see the output of the reconstruction by the k_t algorithm, where the jets have an irregular shape. This is due to the fact that the reconstruction starts with soft particles first as we discussed above. The jets reconstructed with the C/A algorithm shown in the upper right have a very similar jet shape to those from the k_t algorithm. At the bottom of the figure we can see jets reconstructed using the anti-k_t algorithm, which have a very regular shape, which is due to the fact that the algorithm starts with the particles with the highest p_T.

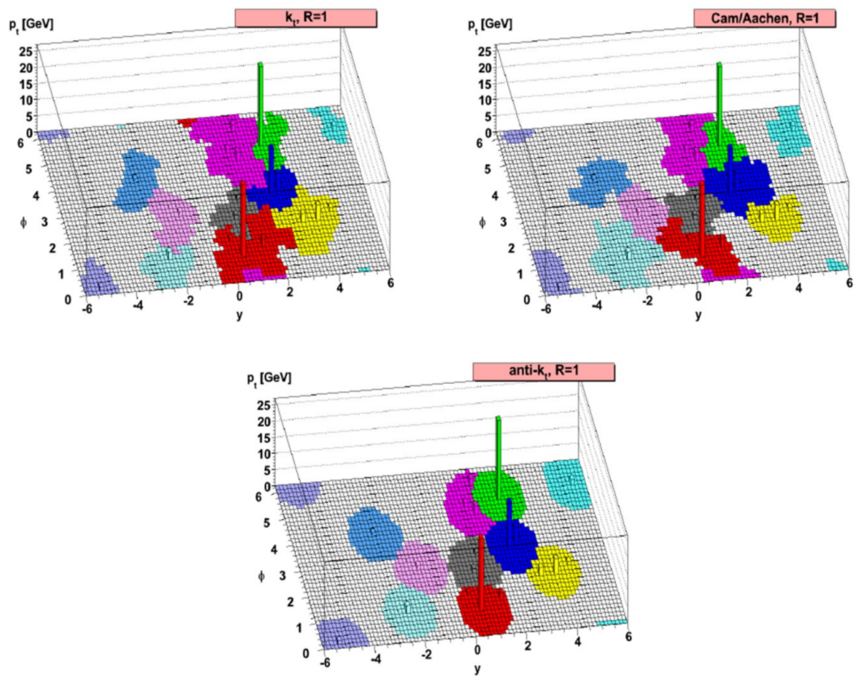

Figure 3.1: Comparison of the use of three different algorithms (top left k_t, top right C/A, down anti-k_t) in a p+p collision with $R = 1$ [23].

Chapter 4

Jet substructure

The study of jet substructure is constantly evolving and expanding. We study the substructure, for example, to determine the origin of the jet, i.e. whether it comes from a quark or a gluon. Furthermore, the substructure can be studied due to jets resulting from the decay of electroweak resonances, such as W, Z and H bosons. Last but not least, the substructure of the jet can be affected by the hot dense medium, which is the topic of this work and will be discussed in more detail in this chapter.

4.1 Tools used to study jet substructure

In order to assess the jet substructure, it is necessary to use techniques that will allow us to do so. Most of these techniques work on the principle of rearranging constituents according to a certain criterion. These techniques can be divided into three groups: Prong finders, Radiation constraints and Groomers.

The first group consists of techniques that seek to find the original parton (prong) from which the jet originated. Thus, these techniques are used primarily to distinguish whether the jet originated classically from a quark or a gluon, or from the decay of electroweak resonance.

The second group focuses mainly on the emission of gluons, according to which it is possible to distinguish the origin of the jet. This is because jets from a quark should emit less gluons than gluon jets.

The third group consists of techniques that focus on the removal of soft radiation along the jet, i.e. the removal of constituents emitted at a large angle and with low transverse momentum. These techniques include the Soft Drop technique, which is used in our analysis and described in more detail below.

4.1.1 Soft Drop

This technique is based on removing soft radiation along the jet. To use the Soft Drop [24] technique, we take a jet of radius R, which was reconstructed using the anti-k_t algorithm. The declusterization of this jet then takes place in the following steps:

1. The jet is reclusterized using the C/A algorithm to get an angulary ordered tree.
2. The jet j is divided into two subjects j_1 a j_2 by undoing the last step of the C/A algorithm.
3. If subjets pass the Soft Drop condition
$$\frac{\min(p_{T,1}, p_{T,2})}{p_{T,1} + p_{T,2}} > z_{cut} \left(\frac{\Delta R_{12}}{R}\right)^{\beta}, \tag{4.1}$$
then the jet j is considered as the final declusterized jet.
4. If the condition is not met, we now denote the subjet with higher transverse momentum p_T as the jet j and repeat the whole process until the condition is met.

The Soft Drop procedure depends on two parameters β and z_{cut}, which are set by the user. The most commonly used values of these parameters are $\beta = 0$ and $z_{cut} = 0.1$

4.2 Jet substructure observables

As already mentioned, this work is mainly focused on the study of the change of jet substructure due to the action of the medium. Quantitatively, this change can be expressed using several observables. We will focus on two observables, the shared momentum fraction z_g and the groomed jet radius R_g, which are both by-products of the Soft Drop technique.

4.2.1 Groomed jet radius R_g

The observable R_g is based on the Soft Drop condition (4.1). The value of R_g corresponds to the first ΔR_{12} that satisfies this condition. It is defined as the angular distance between two branches of splitting, i.e. $R_g = \sqrt{\Delta y^2 + \Delta \psi^2}$. In Fig. 4.1, the observable R_g is plotted for three different values of the parameters z_{cut} and β and different Monte Carlo generators (QPYTHIA [25], JEWEL [26]).

The first named generator, JEWEL, is based on PYTHIA. Using the perturbation method, JEWEL simulates the QCD evolution of jets in a vacuum. In addition, it also simulates the elastic scattering of the partons originated from jet with the medium partons. Jewel can be run in two modes, Recoils on and Recoils off. The first mentioned mode means that partons from the medium that interact with the jet are also counted in the event. They are not counted in the second mode.

Like JEWEL, QPYTHIA is based on the PYTHIA generator. However, it differs in that it models the radiation caused by the medium by means of an increased probability of branching in the jet [27].

In the first graph, the parameters $z_{cut} = 0.1$ and $\beta = 0$ are chosen, which means that the selection of branches is based only on their energies. In the second graph, when choosing the parameters $z_{cut} = 0.5$ and $\beta = 1.5$, we remove such branches that make a large angle with the jet axis. In the last graph, thanks to the choice of parameters $z_{cut} = 0.1$ a $\beta = -1$, we select only hard radiation.

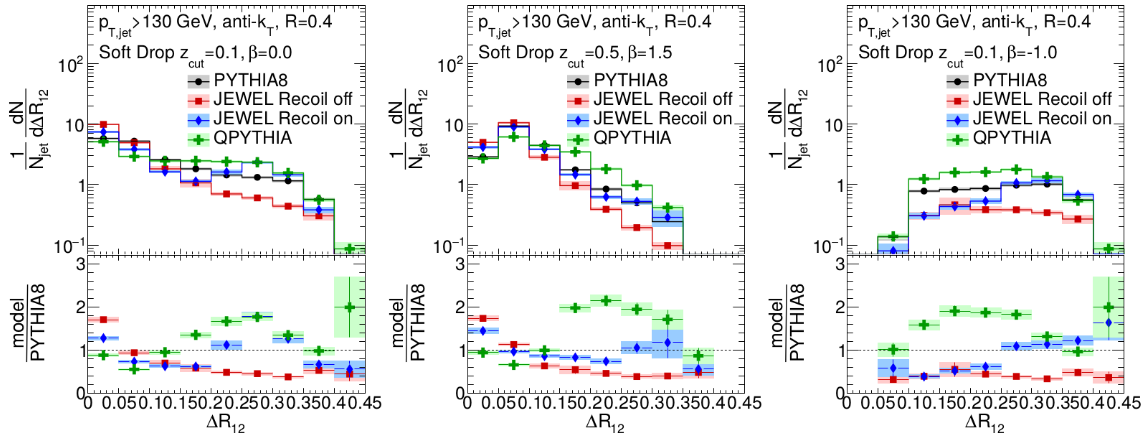

Figure 4.1: ΔR_{12} distribution for three different configurations of parameters z_{cut} and β. At the top of the graphs are simulations from the Monte Carlo JEWEL and QPYTHIA generators and vacuum jets from the PYTHIA8 generator. In the lower part, the ratio of outputs from JEWEL and QPYTHIA generators to PYTHIA8 generator is displayed [28].

4.2.2 Shared momentum fraction z_g

Observable z_g, called *shared momentum fraction* or *jet splitting function*, comes from the Soft Drop condition and is defined by relation

$$z_g = \frac{\min(p_{T,1}, p_{T,2})}{p_{T,1} + p_{T,2}}, \tag{4.2}$$

where $p_{T,i}$ is the transverse momentum of the i-th subjet. It quantifies the proportion of transverse momentum of a less energetic subject to the sum of the momenta of both subjets. The schema of how to obtain this observable is shown in Fig. 4.2.

The observable z_g is plotted in the graphs in Fig. 4.3. As for R_g, three different combinations of z_{cut} and β parameters are used. We can notice that when using different Monte Carlo generators, the curves have the opposite trend. QPYTHIA generates jets wider than vacuum jets, so more jets survive grooming. On the contrary, JEWEL collimates jets, so there are fewer left after grooming. We also see

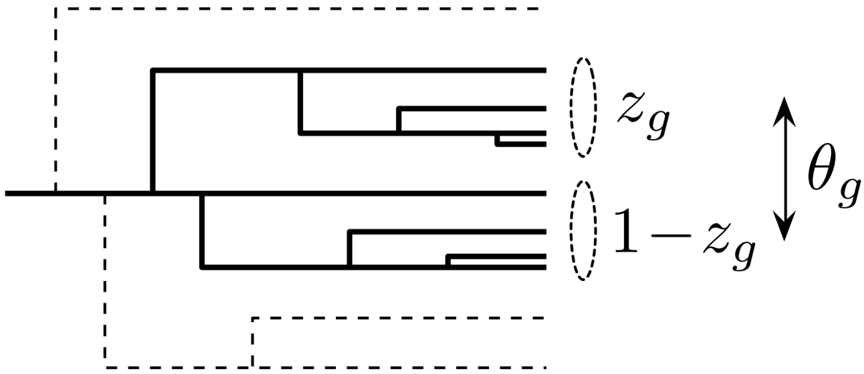

Figure 4.2: Schema of the z_g observable with using the Soft Drop technique. [29].

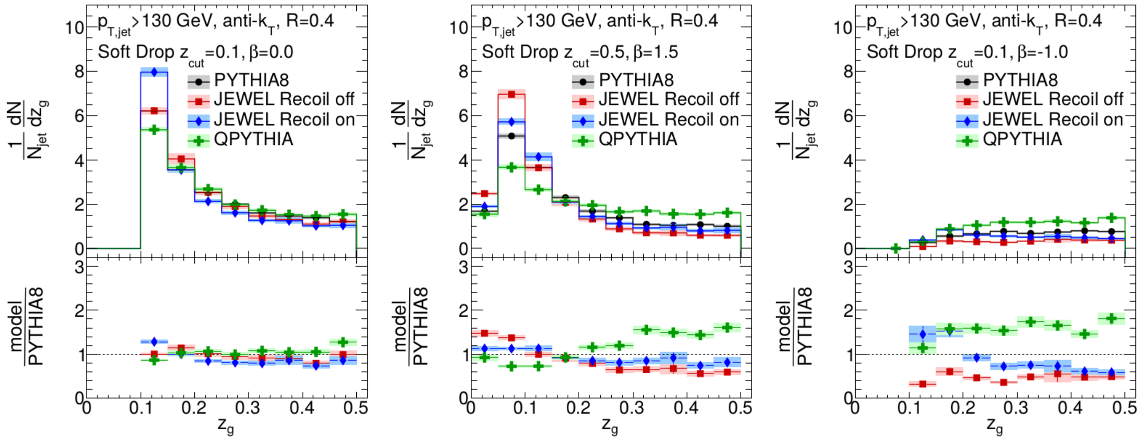

Figure 4.3: Distribution of z_g for three different configurations of parameters z_{cut} and β. At the top of the graphs are simulations from the Monte Carlo JEWEL and QPYTHIA generators and vacuum jets from the PYTHIA8 generator. In the lower part, the ratio of outputs from JEWEL and QPYTHIA generators to PYTHIA8 generator is shown [28].

that when using different modes of the JEWEL generator, the z_g trend does not change much, only in the region of low values.

4.3 Overview of existing results of z_g and R_g measurement

4.3.1 STAR experiment

The latest published results from the measurements observable z_g in the STAR experiment come from data measured in 2006 (p+p) and in 2007 (Au+Au) at energy $\sqrt{s_{NN}} = 200$ GeV.

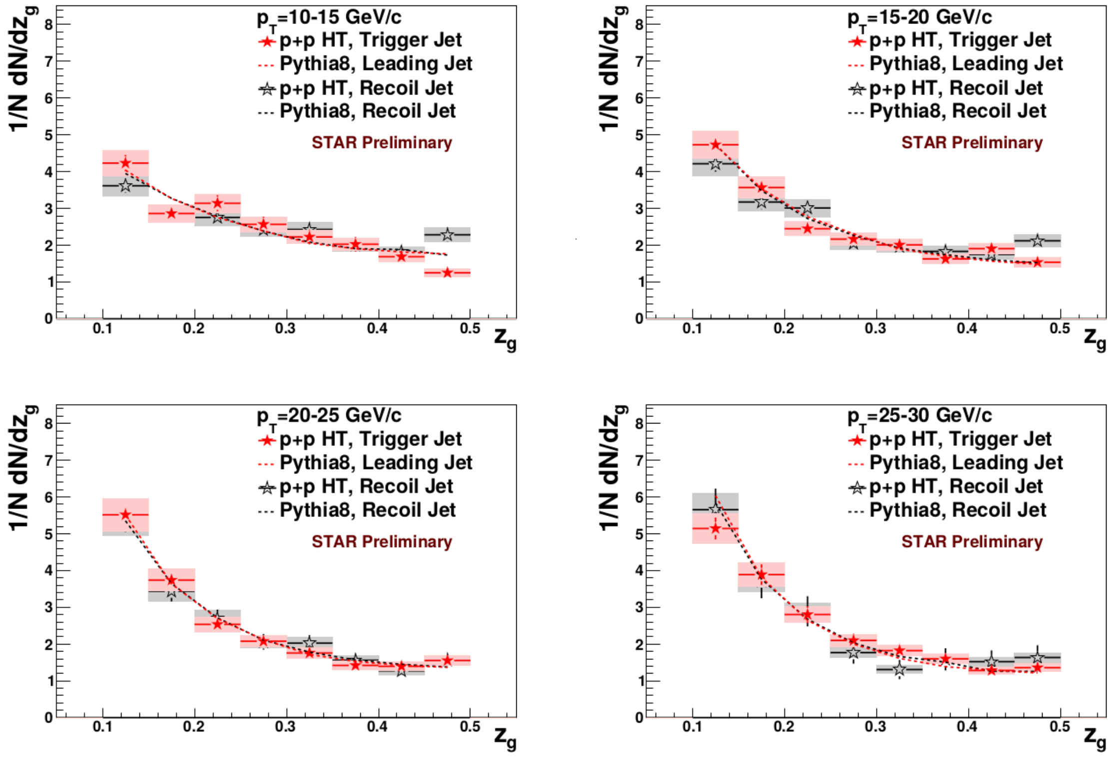

Figure 4.4: z_g distribution for "trigger" and "recoil" jets in p+p collisions at $\sqrt{s} = 200$ GeV and in PYTHIA8 simulations [30].

In the graphs in Fig. 4.4 there are results of z_g for measurements in p+p collisions and simulations for four intervals of transverse momentum of jets. In this analysis, jets are distinguished into "trigger" and "recoil" depending on whether they meet the requirements of the High Tower trigger ($E_T > 5.4$ GeV in at least one BEMC tower). The graphs show the agreement of the measured data with the simulations.

In the graphs in Fig. 4.5 we see z_g distribution this time from central Au+Au collisions at $\sqrt{s_{NN}} = 200$ GeV. On the left is the distribution for "trigger" jets with transverse momentum $p_T^{Trig} = 20 - 30$ GeV/c, on the right is the distribution for "recoil" jets with transverse momentum $p_T^{Recoil} = 10 - 20$ GeV/c. Reference data for this measurement were generated by inserting p+p collisions with HT trigger into Au+Au collisions with minimum-bias trigger.

The ratio of z_g measured in p+p and Au+Au collisions is in the graph in Fig. 4.6. These results do not show a modification of the observable z_g caused by the medium. One reason may be that the selected jets for analysis may have been only slightly modified, or perhaps not at all. Another reason may be the fact that z_g approximates the earliest or hardest branch in the jet, which may be in the area outside the medium.

Newer measurements of z_g and R_g from the STAR experiment come from 2012 from collisions p+p at energy $\sqrt{s} = 200$ GeV.

Fig. 4.7 shows fully corrected z_g distributions for five different transverse momentum

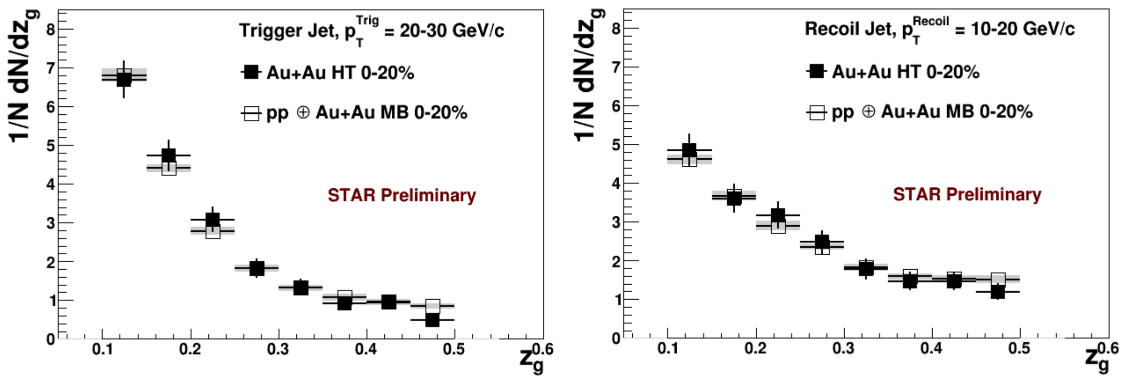

Figure 4.5: z_g distribution of "trigger" (left) and "recoil" (right) jets in Au+Au collisions at $\sqrt{s_{NN}}$ = 200 GeV with 0-20 % centrality. The measured data are compared with reference data p+p HT $\bigoplus$ Au+Au MB [31].

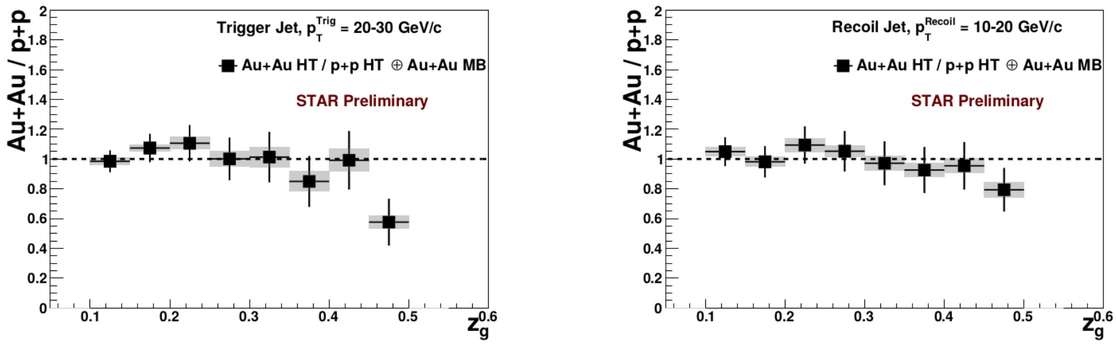

Figure 4.6: z_g ratio in Au+Au and p+p collisions for "trigger" (left) and "recoil" (right) jets [30].

intervals of jets. It can be noticed that for lower transverse momenta we see a larger mean z_g, which means that the splitting is more symmetrical here. The graphs also show simulations from the Monte Carlo generators PYTHIA 6, PYTHIA 8 and HERWIG 7. From the upper parts of the graphs it is clear that all Monte Carlo generators describe the trend of observable z_g. The lower panels show that both PYTHIA versions describe the measurement of z_g quantitatively very well. However, HERWIG 7 shows more symmetric splits, especially for higher $p_{T,jet}$.

In the graphs in Fig. 4.8, the distribution of R_g, as in the case of z_g for five different intervals of centralities, is again compared with the Monte Carlo simulations. Here we see a strong dependence of R_g on the transverse momentum, as the distribution shifts towards lower values with increasing transverse momentum of the jet. In the lower parts of the graph we again see a comparison with Monte Carlo generators, where HERWIG 7 does not describe the region with low R_g very well, while PYTHIA 8, in contrary, the region with higher R_g values. PYTHIA 6 is thus most suitable for the description of observables z_g and R_g.

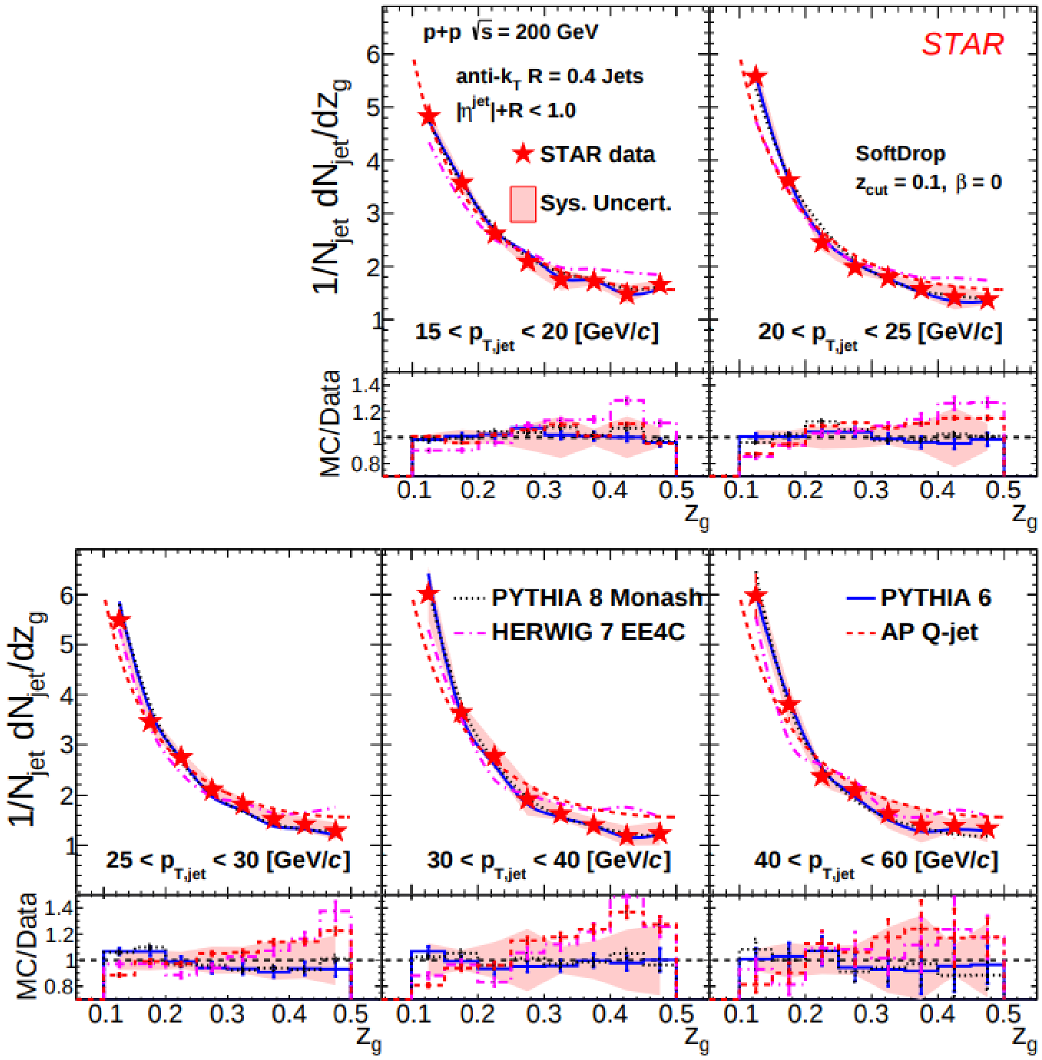

Figure 4.7: Distribution of z_g in p+p collisions at $\sqrt{s}$ = 200 GeV for different transverse momenta of the jets compared with Monte Carlo simulations [32].

4.3.2 CMS experiment

The CMS experiment is located on the LHC accelerator at CERN. The data for the z_g analysis were measured in 2015 in collisions p+p and Pb+Pb at the collision energy $\sqrt{s_{NN}}$ = 5.02 TeV. The transverse momentum requirement of jets in this analysis is $p_{T,jet} > 140$ GeV/c.

In the graph in Fig. 4.9 is the z_g for jets with transverse momentum in the interval 160 GeV/c $< p_{T,jet} <$ 180 GeV/c for 4 different centralities. At the bottom of the graph is the ratio of z_g measurements in Pb+Pb and p+p collisions. While the distribution in the peripheral Pb+Pb collisions corresponds to the reference p+p data, the central Pb+Pb collisions show a steeper z_g distribution. From these results we see that the observable z_g is affected by the medium.

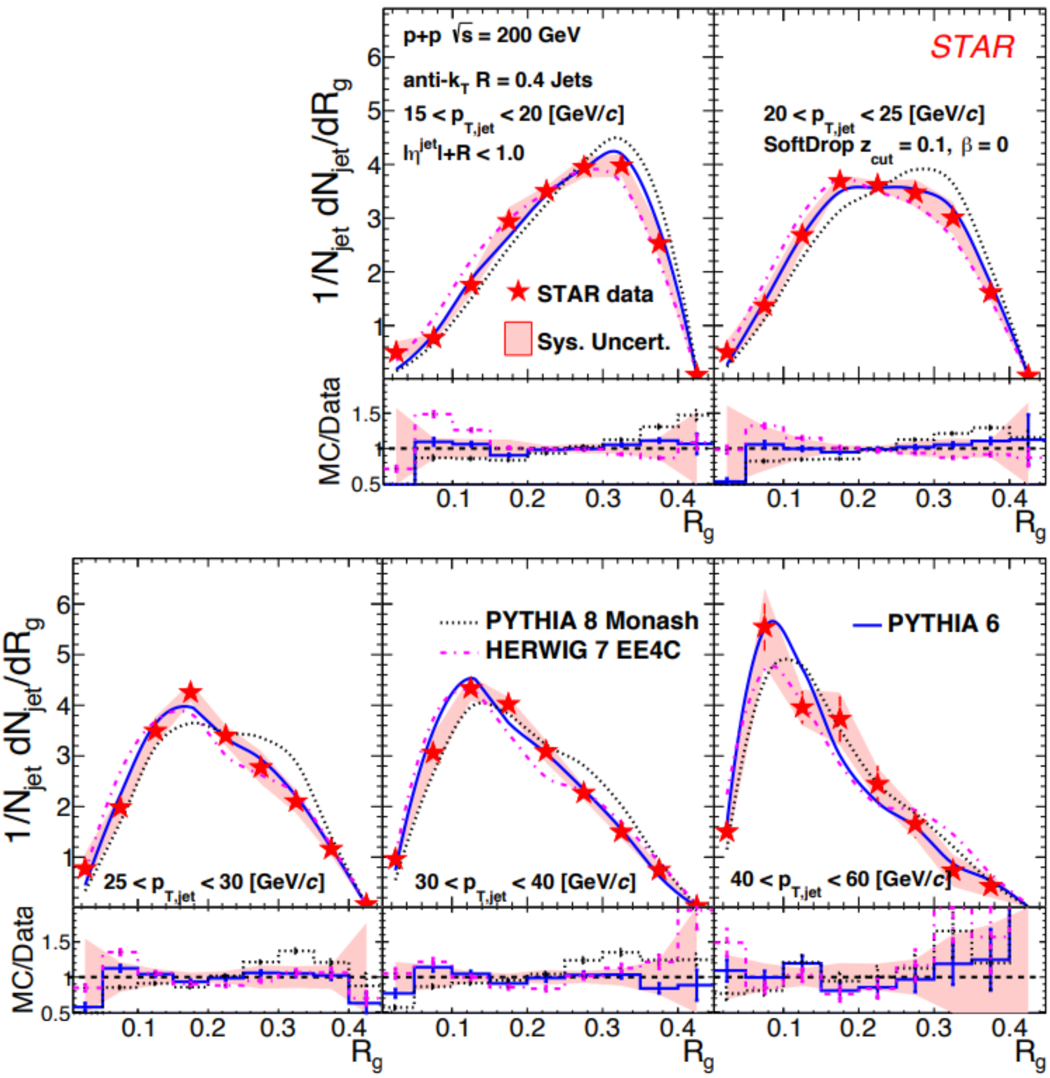

Figure 4.8: Distribution of R_g in p+p collisions at $\sqrt{s}$ = 200 GeV for different transverse momenta of the jets compared with Monte Carlo simulations [32].

4.3.3 ALICE experiment

Probably the latest published results of z_g and R_g measurements come from the ALICE experiment, which, like the CMS, is located at the LHC accelerator at CERN. Data were collected in 2017 at Run2 in p+p collisions at energy $\sqrt{s} = 5.02$ TeV and in 2018 at Run2 in Pb+Pb collisions at energy $\sqrt{s_{NN}} = 5.02$ TeV.

In the graphs in Fig.4.10, the distribution of z_g is in central Pb+Pb (0-10%) collisions. In the left graph, the distribution for the resolution parameter $R = 0.2$ and for charged jets with transverse momentum 60 GeV/c < $p_{T,ch\ jet}$ < 80 GeV/c is shown. In the right graph, the distribution for the resolution parameter $R = 0.4$ and for charged jets with transverse momentum 80 GeV/c < $p_{T,ch\ jet}$ < 100 GeV/c

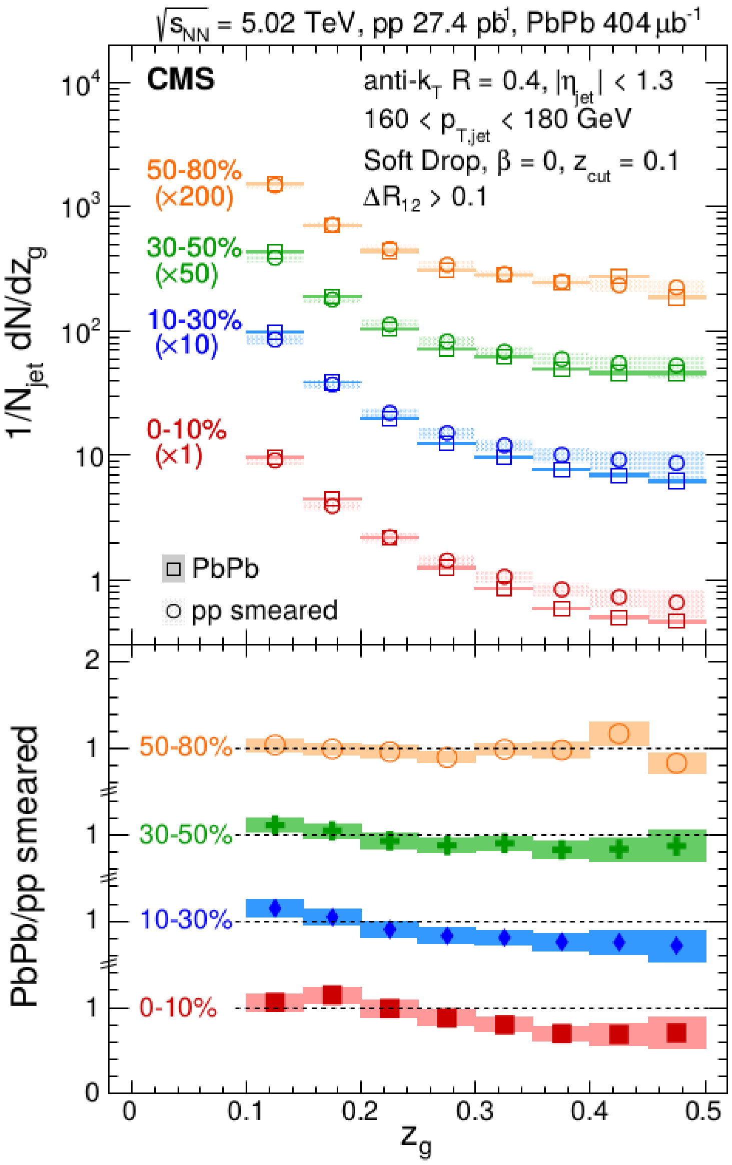

Figure 4.9: Up: z_g distribution in Pb+Pb collisions with $\sqrt{s_{NN}}$ = 2.76 TeV for jets with transverse momentum 160 GeV/c < $p_{T,jet}$ < 180 GeV/c for different centralities. Down: Ratio of z_g distributions in Pb+Pb and p+p collisions [33].

is displayed. In both cases, the values of the parameters of the Soft Drop technique are $z_{cut} = 0.2$ $\beta = 0$. At the bottom of the graphs is the ratio of Pb+Pb collisions to p+p collisions and comparison with models. It can be seen from the graphs that the measurement accuracy decreases with increasing resolution parameter R. The results show no modification in Pb+Pb collisions compared to p+p collisions. At the bottom of the graphs we can see a comparison of the measured data with the following models: JETSCAPE [35], Caucal et al. [36], Chien et al. [37], Qin et al. [38] and Pablos et al. [39–41]. It can be seen from the figure that the data are well described mainly by the model of Caucal et al., which suggests that when implementing the constituents of a vacuum shower into the medium, these constituents then behave

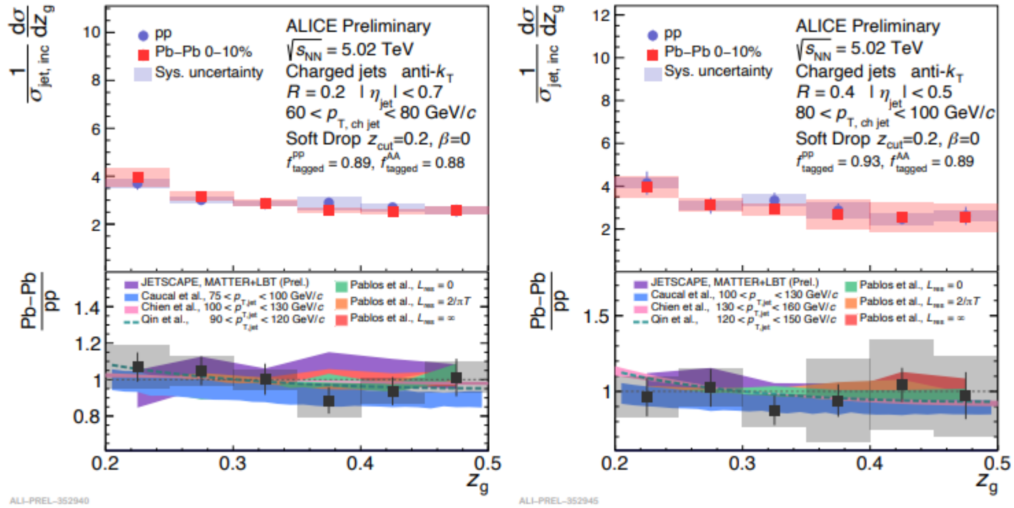

Figure 4.10: Results for z_g in central Pb+Pb collisions at $\sqrt{s_{NN}}$ = 5.02 TeV and p+p collisions for $R = 0.2$, 80 GeV/c < $p_{T,ch\ jet}$ < 100 GeV/c (left) and $R = 0.4$, 80 GeV/c < $p_{T,ch\ jet}$ < 100 GeV/c (right). In the lower part of the graphs, the ratios are compared with theoretical models. [34].

as independent emitters.

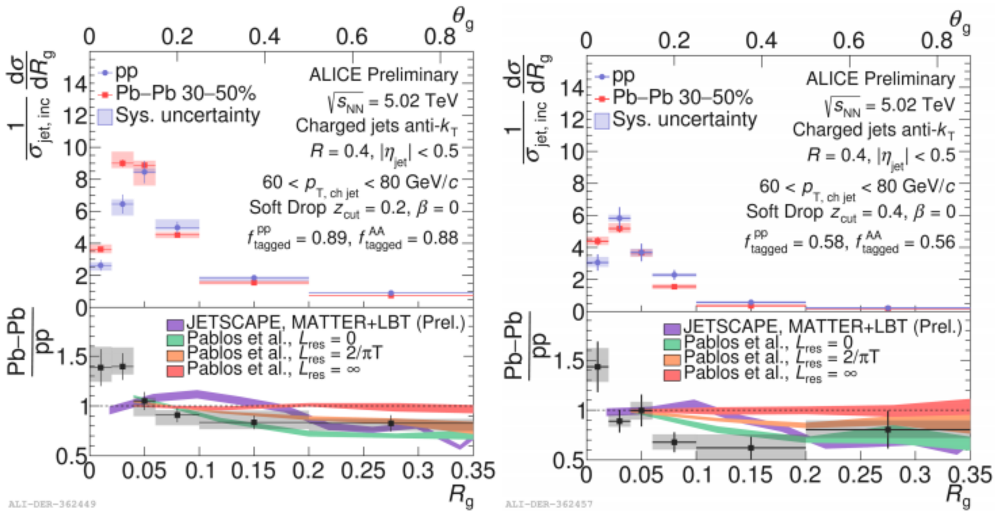

Figure 4.11: Results for R_g in central Pb+Pb collisions at $\sqrt{s_{NN}}$ = 5.02 TeV and p+p collisions for $R = 0.2$, 80 GeV/c < $p_{T,ch\ jet}$ < 100 GeV/c (left) and $R = 0.4$, 80 GeV/c < $p_{T,ch\ jet}$ < 100 GeV/c (right). In the lower part of the graphs, the ratios are compared with theoretical models. [34].

In Fig. 4.11 we can see the distributions for R_g with the same parameters as in the case of z_g distributions. In this case, we see that the R_g distribution in Pb+Pb collisions is narrower than in p+p collisions, which may be the first experimental confirmation of the modification of the angular scale of groomed jets.

Chapter 5

Background subtraction

In heavy ion collisions, a large part of the collected data is an unwanted background. There are several methods to remove this background, each with different properties and uses. Some methods work on the principle of removing the background at the event level, others at the jet level. The methods also differ in whether or not they affect the internal structure of the jet. This chapter will introduce in more detail the methods that were used during the analysis, namely *Area-based subtraction*, *Constituent background subtraction* and *Soft Killer*.

5.1 Area-based subtraction

This method is one of the most commonly used background subtraction methods.

This method consists in correcting the transverse momentum of the jet, $p_{T,jet}^{raw,ch}$, using the jet area A and the medium background density ρ. The correction is given by the relation:

$$p_{T,jet}^{corr,ch} = p_{T,jet}^{raw,ch} - A \cdot \rho, \tag{5.1}$$

where A is the jet area ρ is the medium background density defined as:

$$\rho = \text{med}\left\{\frac{p_{T,jet}^{i}}{A_i}\right\}, \tag{5.2}$$

where i is index over all jets in the event.

As can be seen from Eq. 5.1, using this method, we can subsequently obtain jets with negative transverse momentum.

5.2 Constituent background subtraction

This method represents a generalization of the area-based subtraction. As in the previous method, the background p_T density ρ is used. One way to determine the value of ρ is to divide the event in the $(y - \phi)$ space into rectangular patches. The value of the transverse momentum of each patch $p_{T,patch}$ is then given by this relation:

$$p_{T,patch} = \sum_{i \in patch} p_{T,i}, \tag{5.3}$$

where $p_{T,i}$ is the transverse momentum of the i-th particle in the patch. Background density ρ is then equal to

$$\rho = \text{median}_{patches} \left\{ \frac{p_{T,patch}}{A_{patch}} \right\}. \tag{5.4}$$

There are two possibilities to use this method: **jet-by-jet** or **whole event**.

5.2.1 Jet-by-jet level

When using this method, the jets are clustered first, and then the background is subtracted. This method has the following steps:

1. So-called ghost particles are added to the whole event (Fig. 5.1, top left).
2. Jets are clustered (Fig. 5.1, top right).
3. The transverse momenta p_T of the ghost particles is set to the negative value to correspond to the ρ (Fig. 5.1, down left).
4. Ghosts and particles are matched (Fig. 5.1, down right):
   - First, the distance is determined for each particle(i)-ghost(k) pair:

     $$\Delta R_{i,k} = p_{T,i}^{\alpha} \cdot \sqrt{(y_i - y_k^g)^2 + (\phi_i - \phi_k^g)^2} \tag{5.5}$$

   - We start from the lowest value of $\Delta R_{i,k}$ and combine each particle-ghost pair:
     If $p_{T,i} \geq p_{T,k}^g$:

     $$p_{T,i} \to p_{T,i} - p_{T,k}^g \qquad p_{T,k}^g \to 0 \tag{5.6}$$

     If $p_{T,i} < p_{T,k}^g$:

     $$p_{T,i} \to 0 \qquad p_{T,k}^g \to p_{T,k}^g - p_{T,i} \tag{5.7}$$

- Procedure stops when $\Delta R_{i,k} > \Delta R^{max}$

There are two free parameters in this procedure, α and ΔR^{max}, but varying this parameters has a small effect for this method.

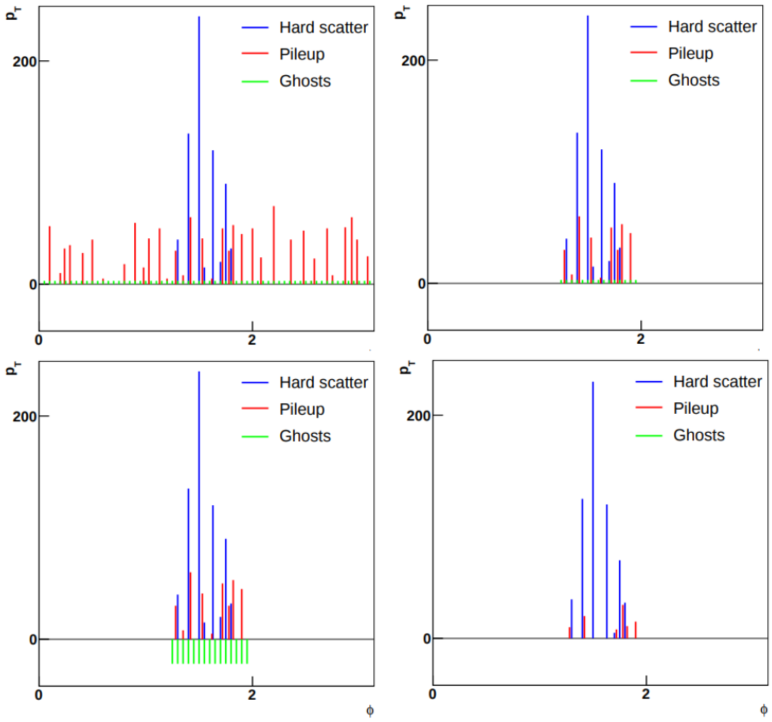

Figure 5.1: Individual steps of the Constituent subtraction method at the jet level. [42].

5.2.2 Whole event level

The application of the constituent subtraction method at the level of whole events is very similar to the application at the jet-by-jet level. Again, it consists of several steps:

1. Ghost particles are added to the whole event (Fig. 5.2, top left).
2. The transverse momenta p_T of the ghost particles is set to the negative value to correspond to the ρ (Fig. 5.2, top right).
3. Ghosts and particles are matched with the same algorithm as for jet-by-jet level (Fig. 5.2).
    - It may happen that some ghosts remain unmatched when the finite ΔR^{max} is chosen (Fig. 5.2).

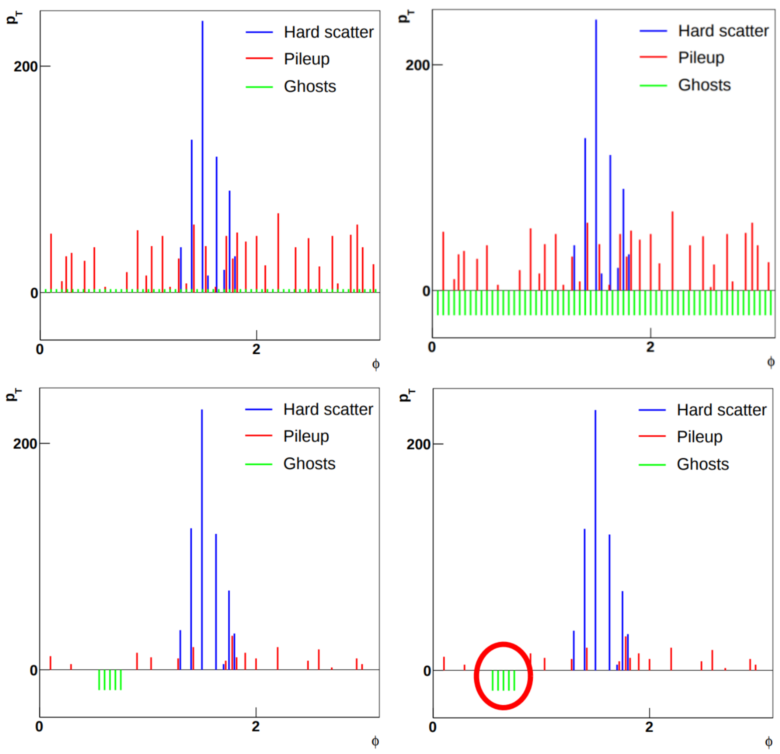

Figure 5.2: Individual steps of the Constituent subtraction method at the whole event level [42].

5.3 SoftKiller

This method works on the principle of removing particles with a transverse momentum p_T less than a given threshold p_T^{cut}.

As in all previous methods, it is necessary to first determine the transverse momentum-flow density ρ. The event is divided in the $(y - \phi)$ space into patches of size $a \times a$. The value of ρ is then defined by the relation:

$$\rho = \text{median}_{i \in patches} \left\{ \frac{p_{T,i}}{A_i} \right\}, \tag{5.8}$$

where $p_{T,i}$ is the transverse momentum of patch i and A_i is the area of patch i.

Then we want to enable p_T^{cut} so that $\rho = 0$, which means that exactly half of the patches are empty. This is illustrated in Fig. 5.3. We can evaluate the p_T^{cut} by determining the particle with the highest transverse momentum $p_{T,i}^{max}$ in each patch, which we then use in relation:

$$p_T^{cut} = \text{median}_{i \in patches} \{p_{T,i}^{max}\}. \tag{5.9}$$

With this choice, it will happen that in the middle of the patches there will be only particles with transverse momentum $p_T < p_T^{cut}$. After applying the threshold, half of the patches will be empty.

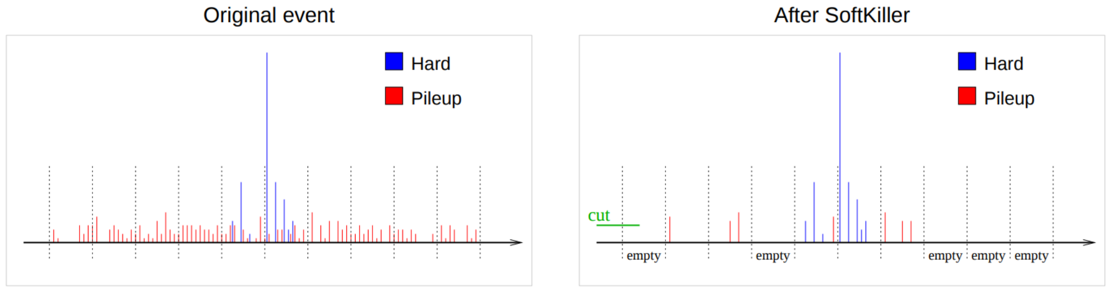

Figure 5.3: Left: Event with hard particles (blue) and pileup particles (red). Right: Event after applying SoftKiller method [43].

Chapter 6

Data analysis

Earlier analyzes of jet production in the STAR experiment were performed on data sets from Au+Au collisions at $\sqrt{s_{NN}} = 200$ GeV Run 7 [44], [30] and Run 11 [21], which have limited statistics (Run 11 contains 1.4 billion events). At present, the analysis is performed mainly on data from Run 14, which has much higher statistics (Run 14 contains ∼10 billion events).

6.1 Reconstruction of Events and Tracks

The data used for this analysis were collected during the Run 14 in Au+Au collisions with energy per nucleon pair $\sqrt{s_{NN}} = 200$ GeV. We are using only data from VPD minimum-bias (MB) triggers to avoid the pile-up events, specifically 450050, 450060, 450005, 450015, 450025.

The analysis is performed on files called picoDst. These files are created from the MuDst files in the pre-analysis, and contain only the most important information about collisions, particle trajectories, and particle identification (PID). These files are used to make the analysis as efficient as possible.

In order for the analysis to be really as efficient as possible and to take place only on such data that we are physically interested in, it is first necessary to apply appropriate selection criteria, so-called cuts, to the data when reconstructing individual events. We consider a suitable event to be an event that meets the condition for the position of the primary vertex, i.e. the place of collision. In our case it is $|z_{vertex}| < 30$ cm from the center of the STAR detector.

We also use selection criteria in the reconstruction of particle tracks. In our case, we primary use information about the tracks of charged particles from the TPC detector. The following cuts for particle tracks are used in this analysis.

1. The minimum number of points at which the particle track is fitted is 14. The maximum number of points that TPC can measure is 45.

2. The ratio of the number of points at which the particle track is fitted to the maximum number of possible fit points is 0.52.

3. Another criterion is the Distance of Closest Approach (DCA) of the track to the primary vertex, which must be less than 1 cm. This excludes tracks originating from secondary decays from the analysis.

4. We require charged particle track momentum in the range 0.2 GeV/$c < p_T <$ 30 GeV/c. This interval is chosen because lower transverse momentum particles cannot provide enough fit points, while particles with higher transverse momentum are almost not curved in the magnetic field and consequently large uncertainty occur in their momentum determination.

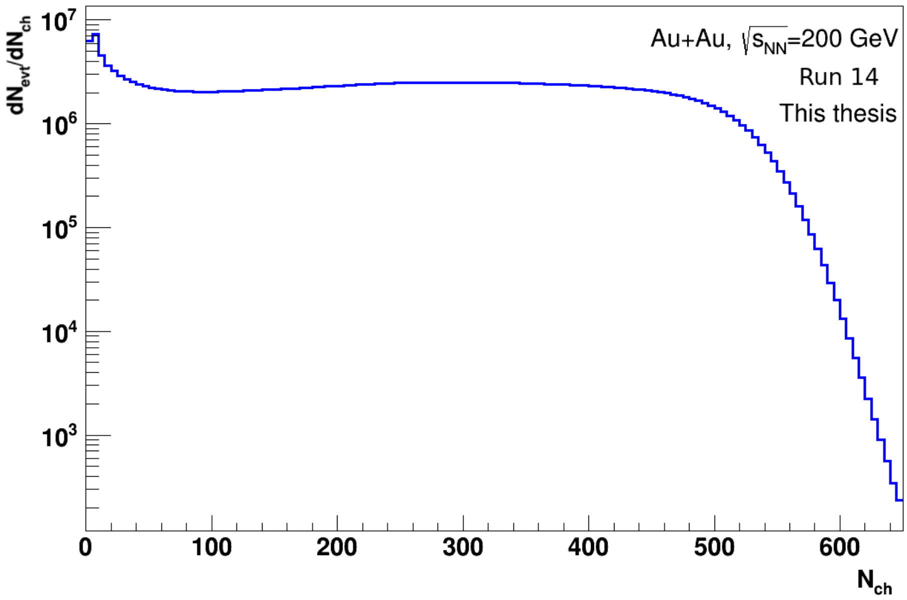

Figure 6.1: Reference multiplicity of charged particles from TPC in Au+Au collisions at energy $\sqrt{s_{NN}}$ = 200 GeV in Run 14.

In Fig. 6.1 we see the reference multiplicity of all charged particles. The shape of this spectrum can be compared with the plot in Fig. 1.1. We see that the shape of the spectrum is similar and we can get the definitions of the classes of centrality from this graph. Table 6.1 shows nine intervals of centralities according to the reference multiplicity of charged particles.

6.2 Jet Reconstruction

The anti-k_t algorithm was used for jet reconstruction, which was described in more detail in the third chapter. The analysis was performed for multiple values of resolution parameters, namely $R \in \{0.2; 0.3; 0.4; 0.5\}$. The jets were reconstructed from

σ/σ_{geo}	N_{ch}
0-5 %	373-441
5-10 %	315-373
10-20 %	263-315
20-30 %	179-263
30-40 %	116-179
40-50 %	71-116
50-60 %	40-71
60-70 %	21-40
70-80 %	10-21

Table 6.1: Table of centrality classes.

the tracks of charged particles with transverse momentum $p_T > 0.2$ GeV/c. At low transverse momentum, clusters of particles can often be reconstructed using the jet algorithm, even though they are not physically jets. Therefore, jets with transverse momentum higher than 10 GeV/c are mostly used in the following graphs. Another criterion we can have on the jet is the minimum value of the transverse momentum $p_{T,lead}$ of the most energetic constituent of the jet. For this analysis, we chose four different values of this cut, namely $p_{T,lead} > \{0, 3, 5, 7\}$ GeV/c. Cuts $p_{T,lead} > 5$ GeV/c and $p_{T,lead} > 7$ GeV/c are commonly used in analyzes. Using these selection criteria, we can minimize background effects.

6.3 Jet Substructure

The main aspect of this thesis is the study of substructure through observables z_g and R_g. These observables can be obtained using the Soft Drop technique [24]. Since the SoftDrop package is not a standard part of the FastJet software [22], it was first necessary to add it and compile it along with the FastJet software. Then I could implement SoftDrop in the code for jet analysis. The subsequent procedure for applying the Soft Drop technique was the same as described in the fourth chapter. Values of $z_{cut} = 0.1$ and $\beta = 0$ were used as input parameters. During the reconstruction, various background subtraction methods, described in Chapter 5, were applied, which are described in the previous chapter.

In the following graphs, the distributions z_g and R_g are presented without background subtraction for different values of the resolution parameter R, for different centralities and for several transverse momentum intervals of jets.

The first pair of graphs in Fig. 6.2 shows the observable R_g for the value of the resolution parameter $R = 0.4$ and the transverse momentum interval 20 GeV/c $< p_T <$ 30 GeV/c for the centralities 0-5 % (left) and 30-40 % (right). From these graphs we see that for the most central collisions the peak is relatively narrow and symmetric, while for peripheral collisions the peak widens and the mean value decreases. In Fig. 6.3 we see the distributions of R_g for the most central collisions (0-5 %) for $R = 0.3$ and 20 GeV/$c < p_T <$ 30 GeV/c (left) and for $R = 0.4$ and

30 GeV/$c < p_T <$ 40 GeV/c (right). On the one hand, we see that with increasing transverse momentum, the statistic decreases, but also with a lower value of the resolution parameter R, i.e. a narrower jet, the peak shifts to lower values.

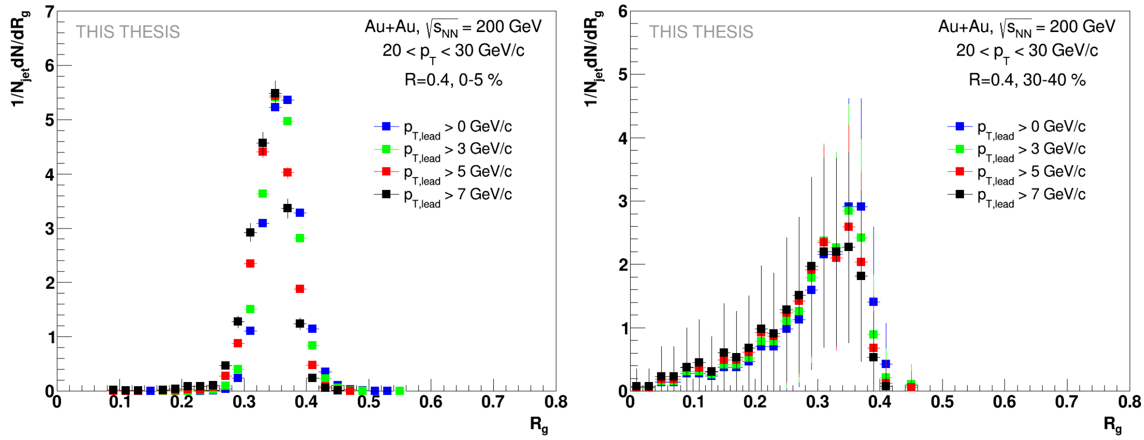

Figure 6.2: R_g distribution for Au+Au collisions with resolution parameter $R = 0.4$ for centrality 0-5 % (left) and 30-40 % (right) for jets in transverse momentum interval 20 GeV/$c < p_T <$ 30 GeV/c.

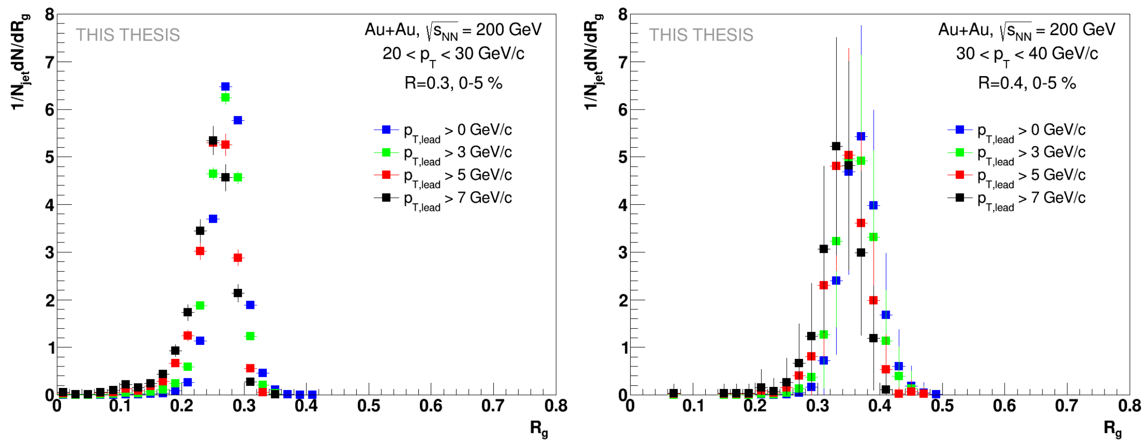

Figure 6.3: R_g distribution for Au+Au most central (0-5 %) collisions with resolution parameter $R = 0.3$ and jet transverse momentum interval 20 GeV/$c < p_T <$ 30 GeV/c (left) and resolution parameter $R = 0.4$ and jet transverse momentum interval 30 GeV/$c < p_T <$ 40 GeV/c (right).

Fig. 6.4 shows graphs of the z_g distribution for the resolution parameter $R = 0.4$ for the interval of the transverse momentum of jets 20 GeV/$c < p_T <$ 30 GeV/c. The distribution for the most central collisions (0-5 %) is plotted on the left and for the peripheral collisions (30-40 %) on the right. We see that in the graph on the right, the distribution for lower values of $p_{T,lead}$, does not have the shape that the observable z_g usually has. This is due to the effects of background. On the contrary, in less central collisions this effect is no longer so noticeable. In Fig. 6.5, we see the

z_g distributions in the most central collisions at the jet interval 20 GeV$/c < p_T <$ 30 GeV$/c$ and the resolution parameter $R = 0.3$ (left), and interval 30 GeV$/c < p_T <$ 40 GeV$/c$ $R = 0.4$ (right). We see that in both cases, the background effects are still quite noticeable.

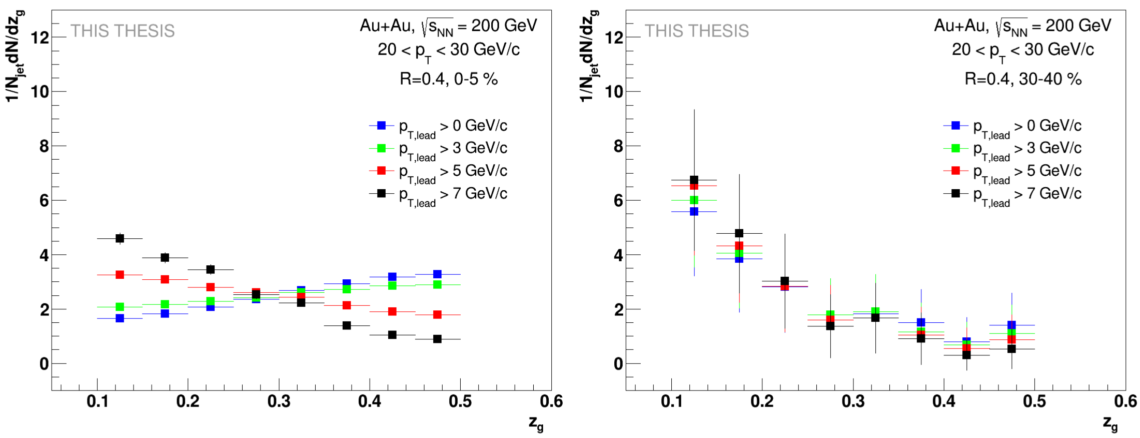

Figure 6.4: z_g distribution for Au+Au collisions with resolution parameter $R = 0.4$ for centrality 0-5 % (left) and 30-40 % (right) for jets in transverse momentum interval 20 GeV$/c < p_T <$ 30 GeV$/c$.

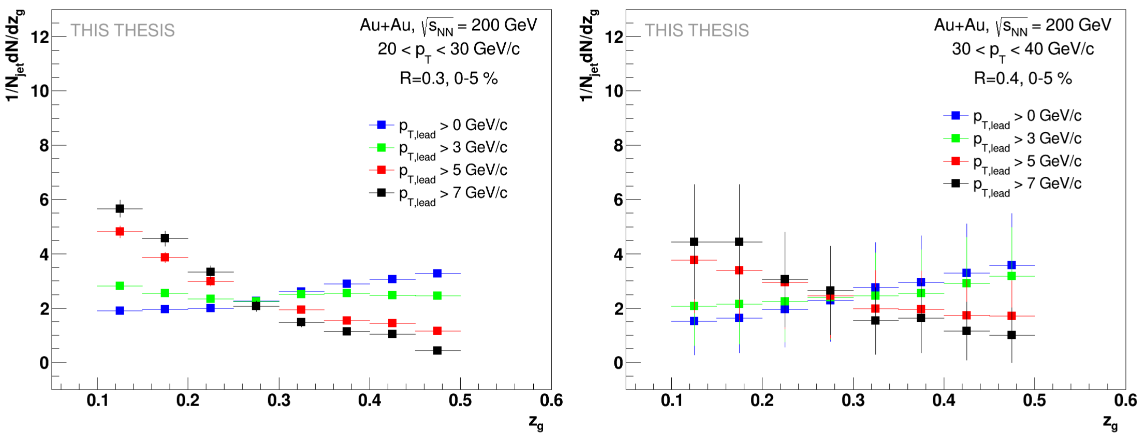

Figure 6.5: z_g distribution for Au+Au most central (0-5 %) collisions with resolution parameter $R = 0.3$ and jet transverse momentum interval 20 GeV$/c < p_T <$ 30 GeV$/c$ (left) and resolution parameter $R = 0.4$ and jet transverse momentum interval 30 GeV$/c < p_T <$ 40 GeV$/c$ (right).

6.3.1 Area-based subtraction

The first method for the background subtraction used is area-based subtraction [45]. As follows from the theoretical introduction of this method in the previous chapter, it is not necessary to enter any input parameters.

Fig. 6.6 shows the R_g distributions of in the most central collisions with jets in the transverse momentum interval 30 GeV$/c$ $< p_T <$ 40 GeV$/c$ for three different values of resolution parameter R. Here it is clear that with increasing resolution parameter, the peak shifts to the right to higher values of R_g. However, the effect of the Area-based subtraction method is not very visible here.

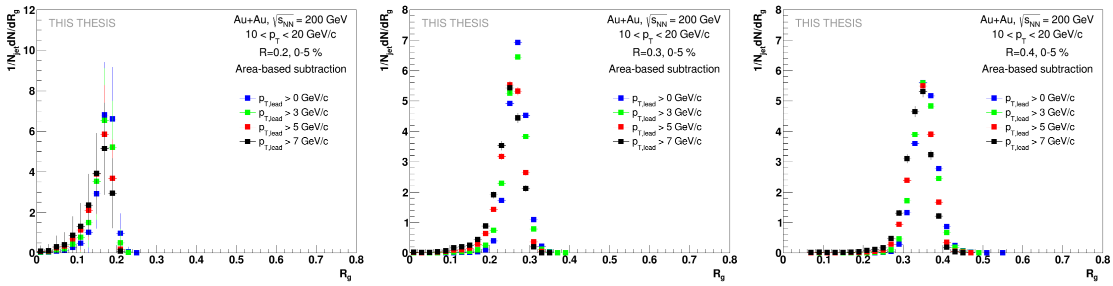

Figure 6.6: R_g distribution for most central (0-5 %) Au+Au collisions collisions with jets in transverse momentum interval 10 GeV$/c$ $< p_T <$ 20 GeV$/c$ with resolution parameter $R = 0.2$ (left), $R = 0.3$ (middle) and $R = 0.4$ (right).

The observable z_g shows a much better sensitivity to the area-based background subtraction. From the graphs in Fig. 6.7 for the most central collisions, the transverse momentum of jets in the interval 20 GeV$/c$ $< p_T <$ 30 GeV$/c$ and the resolution parameters $R = 0.3$ (left) and $R = 0.4$ (right) we see that they bring our expectations closer. On the other hand, the spectra are slightly "jagged ", which may be due to lower statistics caused by the application of the background subtraction method.

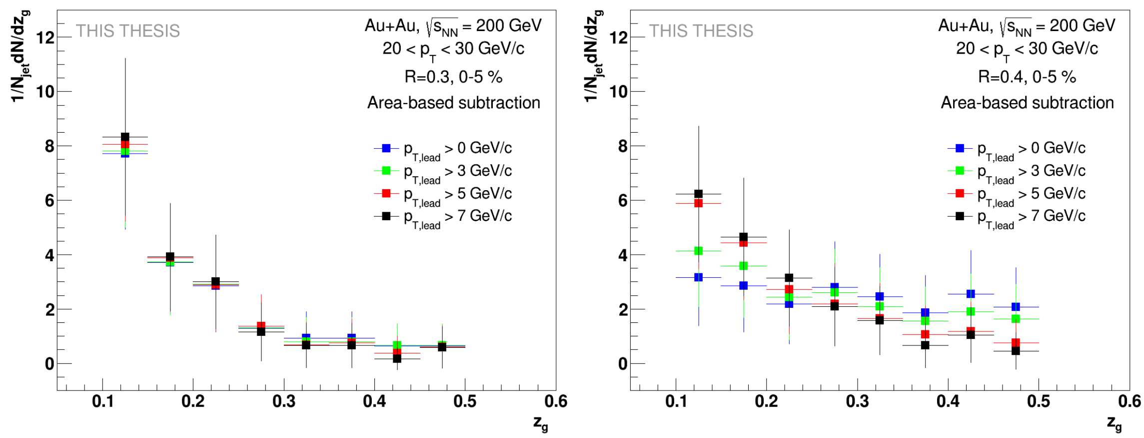

Figure 6.7: z_g distribution for most central Au+Au collisions for jets in transverse momentum interval 20 GeV$/c$ $< p_T <$ 30 GeV$/c$ with resolution parameter $R = 0.3$ (left) and $R = 0.4$ (right).

6.3.2 Constituent background subtraction

Jet-by-jet level

This method is used directly at the jet level and requires the input of two free parameters, which I have chosen as $\alpha = 2$ and $\Delta R^{max} = 0.5$ according to general practice.

Fig. 6.8 shows two graphs of the R_g distribution for the resolution parameter $R = 0.4$ in central (0-5 %) collisions for jets with transverse momentum in the interval 20 GeV/c $< p_T <$ 30 GeV/c (left) and in peripheral (30-40 %) collisions for jets with transverse momentum in the interval 10 GeV/c $< p_T <$ 20 GeV/c. In these graphs, the rising second peak, which we would expect in these places, is evident in the lower values of R_g.

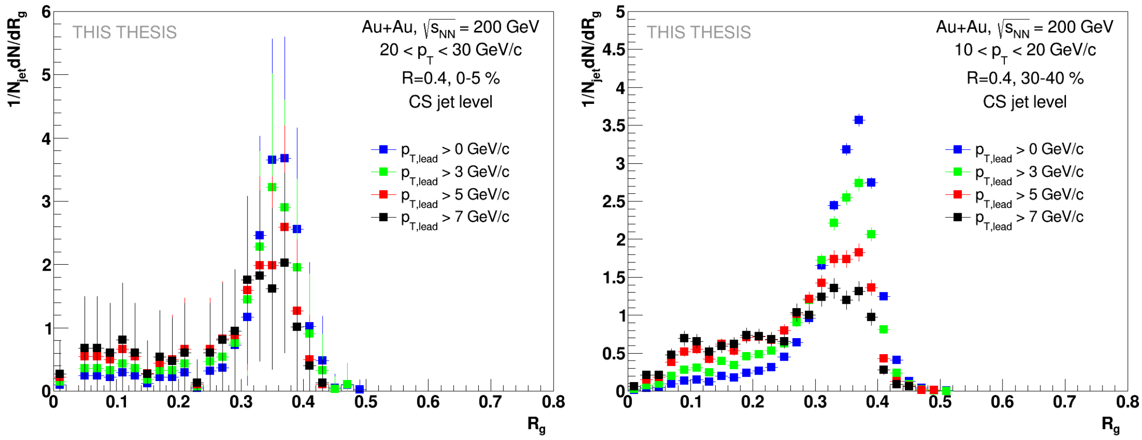

Figure 6.8: R_g distribution for Au+Au collisions with resolution parameter $R = 0.4$ for centrality 0-5 % and jets in transverse momentum interval 10 GeV/c $< p_T <$ 20 GeV/c (left), and 30-40 % and jets in transverse momentum interval 20 GeV/c $< p_T <$ 30 GeV/c (right).

In Fig. 6.9 the z_g distribution are shown for the resolution parameter $R = 0.4$ in central (0-5 %) collisions for jets with transverse momentum in the interval 20 GeV/c $< p_T <$ 30 GeV/c (left) and in peripheral (30-40 %) collisions for jets with transverse momentum in the interval 10 GeV/c $< p_T <$ 20 GeV/c. We see that both distributions have a trend that we would expect, but the spectra are again slightly fluctuating.

Whole event level

In this variant of the constituent background subtraction method, I chose the input parameters as $\alpha = 0$ and $\Delta R^{max} = 0.05$.

In the graphs in Fig. 6.10 is the R_g distribution for the most central collisions with the resolution parameter $R = 0.4$ and jets with transverse momentum in intervals

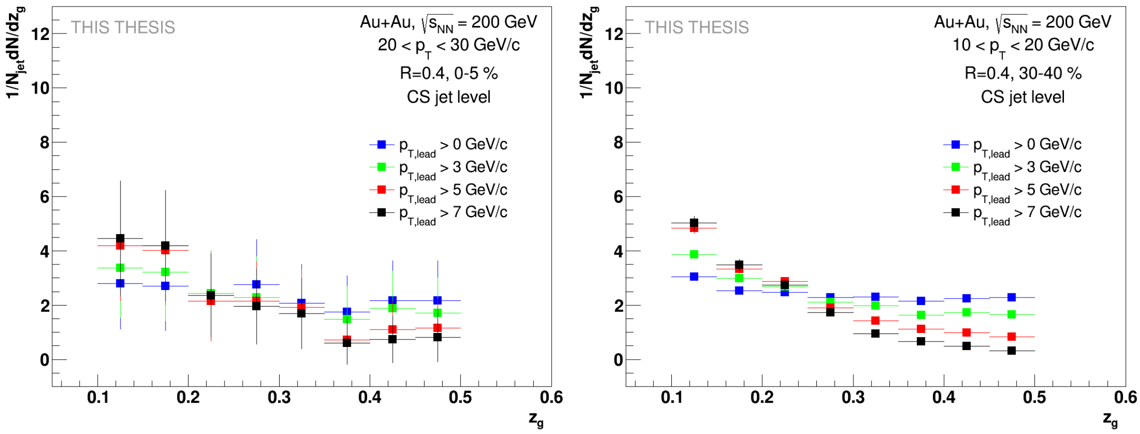

Figure 6.9: z_g distribution for Au+Au collisions with resolution parameter $R = 0.4$ for centrality 0-5 % and jets in transverse momentum interval 10 GeV$/c < p_T <$ 20 GeV$/c$ (left), and 30-40 % and jets in transverse momentum interval 20 GeV$/c$ $< p_T <$ 30 GeV$/c$ (right).

10 GeV$/c < p_T <$ 20 GeV$/c$ (left) and 20 GeV$/c < p_T <$ 30 GeV$/c$ (right). We see that using this method, we have prepared a fairly large part of the statistics, yet we see a similar trend in jets with low lateral momentum as in previous cases. Due to low statistics, not all cuts on $p_{T,lead}$ are used.

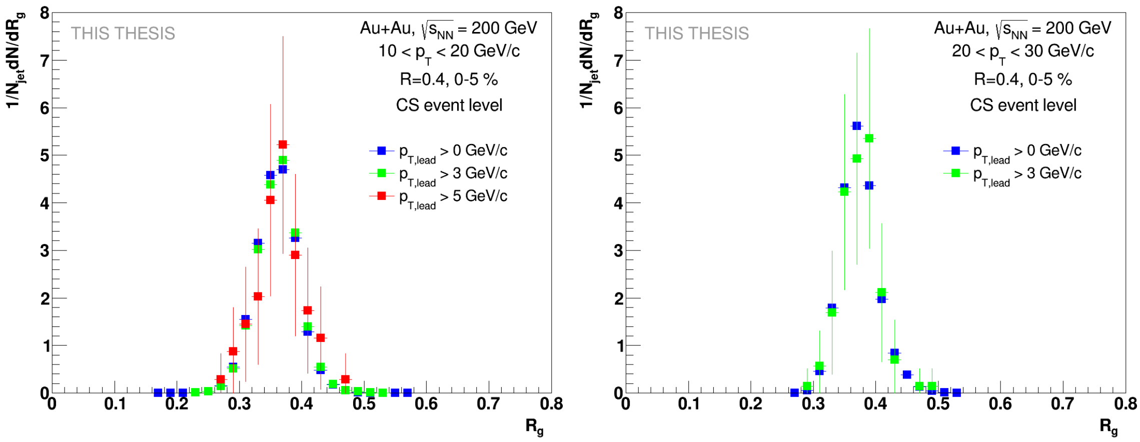

Figure 6.10: R_g distribution for Au+Au most central collisions with resolution parameter $R = 0.4$ for jets in transverse momentum interval 10 GeV$/c < p_T <$ 20 GeV$/c$ (left) and 20 GeV$/c < p_T <$ 30 GeV$/c$ (right).

Fig. 6.11 shows the z_g distribution for the most central collisions with the resolution parameter $R = 0.4$ and jets with transverse momentum in intervals 10 GeV$/c < p_T$ $<$ 20 GeV$/c$ (left) and 20 GeV$/c < p_T <$ 30 GeV$/c$ (right). We see that when using this method we get the opposite trend than when using other methods. As with R_g, not all cuts on $p_{T,lead}$ are used due to low statistics.

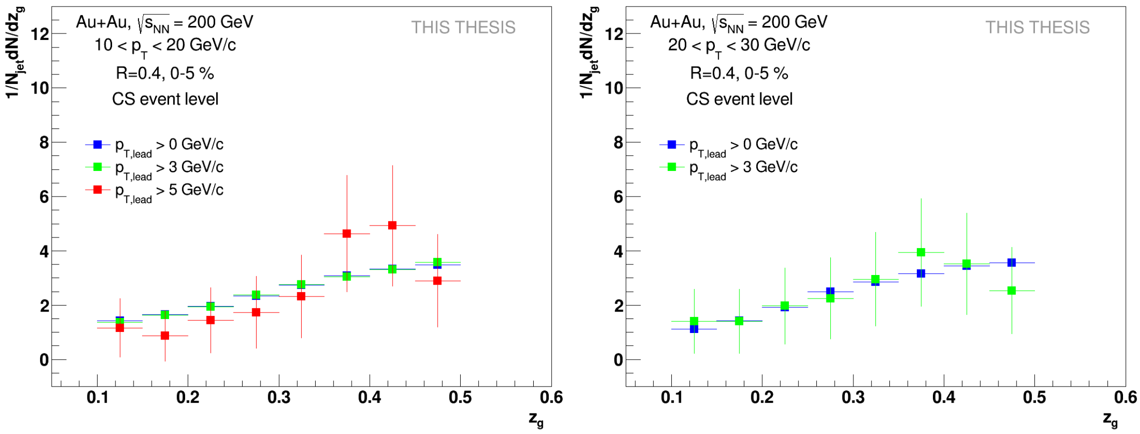

Figure 6.11: z_g distribution for Au+Au most central collisions with resolution parameter $R = 0.4$ for jets in transverse momentum interval 10 GeV$/c < p_T <$ 20 GeV$/c$ (left) and 20 GeV$/c < p_T <$ 30 GeV$/c$ (right).

6.3.3 SoftKiller

In this method, we choose the patch size parameter a. In our analysis, we chose this parameter according to the general conventions $a = 0.4$.

Unfortunately, using this method has significantly reduced statistics. In the graphs in Fig. 6.12, for the most central collisions with the resolution parameter $R = 0.5$ for jets in the interval 10 GeV$/c < p_T <$ 20 GeV$/c$, the R_g distribution is on the left and the z_g distribution on the right. Due to low statistics, only distributions for $p_{T,lead} > 0$ GeV$/c$ and $p_{T,lead} > 3$ GeV$/c$ are plotted. Due to low statistics, we also see significant fluctuations.

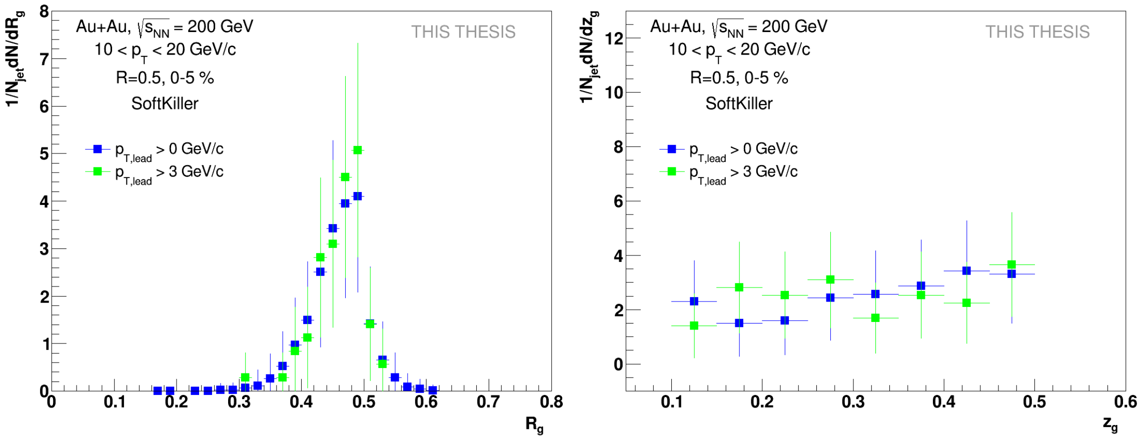

Figure 6.12: R_g (left) and z_g (right) distribution for Au+Au collisions with resolution parameter $R = 0.5$ for centrality 0-5 % and jets in transverse momentum interval 10 GeV$/c < p_T <$ 20 GeV$/c$ (left).

Summary

Jets can serve as a good probe for studying quark-gluon plasma, which is formed in heavy ion collisions at high energies. The medium can affect the inclusive properties and substructure of jets. In recent years, the study of substructure has become increasingly popular due to the growing statistics of measured data. The substructure of jets is also the main topic of this work.

In the theoretical part of the work, I got acquainted with the origin and properties of quark-gluon plasma and with the collisions of heavy ions in which QGP is formed.

I also gained knowledge about RHIC and the STAR experiment, located at RHIC. I got familiar with the principle of operation of individual subdetectors of the STAR experiment, which was important for the subsequent analysis of data.

It was also essential to get an overview of jets, their reconstruction and also the substructure and techniques that are associated with these studies. I mainly focused on observables z_g and R_g. Furthermore, some methods of background subtraction are introduced, which are then applied in the practical part of the work.

In the practical part of the work, I performed an analysis on data from 2014 from Au+Au collisions at energy $\sqrt{s_{NN}} = 200$ GeV measured by the STAR experiment. Reconstruction of jets was performed, application of three methods to background subtraction and subsequent extraction of uncorrected spectra of observables z_g and R_g. From the graphs it can be concluded that they have the same qualitative trend as the results published so far. From the given distributions, it seems that in the study of the substructure, methods that are applied at the level of jets, rather than whole events, are more suitable.

In the next phases of the analysis, the aim will be to create corrected spectra and to focus even more and qualitatively evaluate the background subtraction methods.

Bibliography

[1] R. Snellings, "Elliptic flow," *New Journal of Physics*, vol. 13, no. 5, 2011-05-01. [Online]. Available: http://stacks.iop.org/1367-2630/13/i=5/a=055008?key=crossref.c773a93ac52a394972a8dd339d789698

[2] M. L. Miller, "Glauber Modeling in High-Energy Nuclear Collisions," *Annual Review of Nuclear and Particle Science*, vol. 57, no. 1, pp. 205–243, 2007. [Online]. Available: http://www.annualreviews.org/doi/10.1146/annurev.nucl.57.090506.123020

[3] K. Yagi, *Quark-gluon Plasma.* Cambridge University Press, 2005.

[4] L. Kumar and D. Keane, "Experimental studies of the quantum chromodynamics phase diagram at the STAR experiment," *Pramana*, vol. 84, no. 5, pp. 773–786, 2015. [Online]. Available: http://link.springer.com/10.1007/s12043-015-0969-9

[5] S. Sarkar, *The physics of the Quark-Gluon plasma.* New York: Springer, c2010.

[6] S. Campbell, "SPHENIX," *Journal of Physics: Conference Series*, vol. 832, 2017-04-25. [Online]. Available: http://stacks.iop.org/1742-6596/832/i=1/a=012012?key=crossref.5f8da25addfdbde762d6fb42c0974640

[7] F. Meot. (2019) The Electron-Ion Collider eRHIC. IAS HEP Conference, HKUST. [Online]. Available: http://ias.ust.hk/program/shared_doc/2019/201901hep/conf/20190121_LT_pm_Francois%20Meot.pdf

[8] Brookhaven National Laboratory. [Online]. Available: https://www.bnl.gov/about/

[9] D. Arkhipkin and J. Lauret, "STAR Online Meta-Data Collection Framework," *Journal of Physics: Conference Series*, vol. 898, p. 7, 2017-10-01. [Online]. Available: http://stacks.iop.org/1742-6596/898/i=3/a=032023?key=crossref.464ab7be30f00bd0a49430f262d3d35a

[10] M. Anderson, et al., "The STAR time projection chamber," *Nuclear Instruments and Methods in Physics Research Section A: Accelerators, Spectrometers, Detectors and Associated Equipment*, vol. 499, no. 2-3, pp. 659–678, 2003. [Online]. Available: https://linkinghub.elsevier.com/retrieve/pii/S0168900202019642

[11] X. Dong, "The Time-Of-Flight Detector for RHIC/STAR and The Related Physics," *AIP Conference Proceedings*, pp. 332–337, 2006. [Online]. Available: http://aip.scitation.org/doi/abs/10.1063/1.2398870

[12] T. M. Cormier, et al., "STAR barrel electromagnetic calorimeter absolute calibration using "minimum ionizing particles" from collisions at RHIC," *Nuclear Instruments and Methods in Physics Research Section A: Accelerators, Spectrometers, Detectors and Associated Equipment*, vol. 483, no. 3, pp. 734–746, 2002. [Online]. Available: https://linkinghub.elsevier.com/retrieve/pii/S0168900201019519

[13] The STAR Experiment. [Online]. Available: https://drupal.star.bnl.gov/STAR

[14] C. E. Allgower, et al., "The STAR Endcap Electromagnetic Calorimeter," *Nuclear Instruments and Methods in Physics Research Section A: Accelerators, Spectrometers, Detectors and Associated Equipment*, vol. 499, no. 2-3, p. 15, 2003.

[15] C. A. Whitten, "The Beam-Beam Counter," *AIP Conference Proceedings*, pp. 390–396, 2008. [Online]. Available: http://aip.scitation.org/doi/abs/10.1063/1.2888113

[16] W. J. Llope, et al., "The STAR Vertex Position Detector," *Nuclear Instruments and Methods in Physics Research Section A: Accelerators, Spectrometers, Detectors and Associated Equipment*, vol. 759, p. 18, 2014.

[17] C. Adler, et al., "The RHIC zero degree calorimeters," *Nuclear Instruments and Methods in Physics Research Section A: Accelerators, Spectrometers, Detectors and Associated Equipment*, vol. 470, no. 3, pp. 488–499, 2001. [Online]. Available: https://linkinghub.elsevier.com/retrieve/pii/S0168900201006271

[18] H. Qiu, "STAR heavy flavor tracker," *Nuclear Physics A*, vol. 931, pp. 1141–1146, 2014. [Online]. Available: https://linkinghub.elsevier.com/retrieve/pii/S0375947414003157

[19] Heavy Flavor Tracker for STAR. [Online]. Available: https://www.bnl.gov/newsroom/news.php?a=24657

[20] J. Kapitán, "Jets in heavy ion collisions at RHIC," p. 5, 2009.

[21] J. Rusňák, "Jet Reconstruction in Au+Au Collisions at RHIC," 2017. [Online]. Available: https://drupal.star.bnl.gov/STAR/files/phd_thesis_rusnak.pdf

[22] M. Cacciari, G. P. Salam and G. Soyez, "FastJet user manual," *The European Physical Journal C*, vol. 72, no. 3, 2012. [Online]. Available: http://link.springer.com/10.1140/epjc/s10052-012-1896-2

[23] R. Atkin, "Review of jet reconstruction algorithms," *Journal of Physics: Conference Series*, vol. 645, 2015-10-15. [Online]. Available: http://stacks.iop.org/1742-6596/645/i=1/a=012008?key=crossref.cf7670068f29afdafa203db94719fd66

[24] A. J. Larkoski, S. Marzani, G. Soyez and J. Thaler, "Soft drop," *Journal of High Energy Physics*, vol. 2014, no. 5, 2014. [Online]. Available: http://link.springer.com/10.1007/JHEP05(2014)146

[25] N. Armesto, L. Cunqueiro and C. A. Salgado, "Q-PYTHIA," *The European Physical Journal C*, vol. 63, no. 4, pp. 679–690, 2009. [Online]. Available: http://www.springerlink.com/index/10.1140/epjc/s10052-009-1133-9

[26] K. Zapp, "JEWEL 2.0.0," *The European Physical Journal C*, vol. 74, no. 2, 2014. [Online]. Available: http://link.springer.com/10.1140/epjc/s10052-014-2762-1

[27] M. van Leeuwen, "Jet Fragmentation and Jet Shapes in JEWEL and q-PYTHIA," *Nuclear and Particle Physics Proceedings*, vol. 276-278, pp. 293–296, 2016. [Online]. Available: http://linkinghub.elsevier.com/retrieve/pii/S2405601416301018

[28] H. A. Andrews, et al., "Novel tools and observables for jet physics in heavy-ion collisions," 2018.

[29] A. Larkoski, S. Marzani, J. Thaler, A. Tripathee and W. Xue, "Exposing the QCD Splitting Function with CMS Open Data," *Physical Review Letters*, vol. 119, no. 13, 2017. [Online]. Available: https://link.aps.org/doi/10.1103/PhysRevLett.119.132003

[30] K. Kauder, "Measurement of the Shared Momentum Fraction z_g using Jet Reconstruction in p+p and Au+Au Collisions with STAR," *Nuclear and Particle Physics Proceedings*, vol. 289-290, pp. 137–140, 2017. [Online]. Available: https://linkinghub.elsevier.com/retrieve/pii/S2405601417302171

[31] ——, "Measurement of the Shared Momentum Fraction z_g using Jet Reconstruction in p+p and Au+Au Collisions with STAR," 2017. [Online]. Available: https://indico.cern.ch/event/433345/contributions/2358470/

[32] J. Adam, et al., "Measurement of Groomed Jet Substructure Observables in p+p Collisions at $\sqrt{s_{NN}}$= 200 GeV with STAR," 2020-03-04. [Online]. Available: https://arxiv.org/pdf/2003.02114.pdf

[33] A.M. Sirunyan, et al., "Measurement of the splitting function in pp and PbPb collisions at $\sqrt{s_{NN}} = 5.02$ TeV," *Physical Review Letters*, vol. 120, no. 14, 2018.

[34] ALICE Collaboration, "Measurements of the groomed jet radius and groomed momentum fraction in pp and Pb-Pb collisions at $\sqrt{s_{NN}} = 5.02$ TeV," 2020-07-30. [Online]. Available: http://cds.cern.ch/record/2725572/files/ALICE_public_note.pdf?version=2

[35] e. a. JETSCAPE Collaboration, J. Putschke, "The JETSCAPE framework." [Online]. Available: arXiv:1903.07706[nucl-th]

[36] P. Caucal, E. Iancu and G. Soyez, "Deciphering the z_g distribution in ultrarelativistic heavy ion collisions," *Journal of High Energy Physics*, p. 273, 2019. [Online]. Available: https://doi.org/10.1007/JHEP10(2019)273

[37] Y.-T. Chien and I. Vitev, “Probing the Hardest Branching within Jets in Heavy-Ion Collisions,” *Physical Review Letters*, vol. 119, no. 11, 2017. [Online]. Available: https://link.aps.org/doi/10.1103/PhysRevLett.119.112301

[38] N.-B. Chang, S. Cao and G.-Y. Qin, “Probing medium-induced jet splitting and energy loss in heavy-ion collisions,” *Physics Letters B*, vol. 781, pp. 423–432, 2018. [Online]. Available: https://linkinghub.elsevier.com/retrieve/pii/S0370269318303034

[39] Z. Hulcher, D. Pablos and K. Rajagopal, “Resolution effects in the hybrid strong/weak coupling model,” *Journal of High Energy Physics*, vol. 2018, no. 3, 2018. [Online]. Available: http://link.springer.com/10.1007/JHEP03(2018)010

[40] J. Casalderrey-Solana, D. C. Gulhan, J. G. Milhano, D. Pablos and K. Rajagopal, “A hybrid strong/weak coupling approach to jet quenching,” *Journal of High Energy Physics*, vol. 2014, no. 10, 2014. [Online]. Available: http://link.springer.com/10.1007/JHEP10(2014)019

[41] J. Casalderrey-Solana, G. Milhano, D. Pablos and K. Rajagopal, “Modification of jet substructure in heavy ion collisions as a probe of the resolution length of quark-gluon plasma,” *Journal of High Energy Physics*, vol. 2020, no. 1, 2020. [Online]. Available: http://link.springer.com/10.1007/JHEP01(2020)044

[42] P. Berta, L. Masetti, D. Miller and M. Spousta, “Constituent Subtraction Updates,” 2018. [Online]. Available: https://indico.cern.ch/event/649482/contributions/2993293/attachments/1687676/2714424/PeterBerta_CS_17.7.2018.pdf

[43] M. Cacciari, G. P. Salam and G. Soyez, “SoftKiller, a particle-level pileup removal method,” *The European Physical Journal C*, vol. 75, no. 2, 2015. [Online]. Available: http://link.springer.com/10.1140/epjc/s10052-015-3267-2

[44] L. Adamczyk, et al., “Dijet imbalance measurements in Au+Au and p+p collisions at $\sqrt{s_{NN}} = 200$ GeV at STAR,” *Physical Review Letters*, vol. 119, no. 6, 2017.

[45] M. Cacciari, G. P. Salam and G. Soyez, “The catchment area of jets,” *Journal of High Energy Physics*, vol. 2008, no. 04, pp. 005–005, 2008-04-01. [Online]. Available: http://stacks.iop.org/1126-6708/2008/i=04/a=005?key=crossref.2f6f89a18d40d59672b117f8023f0678